Shifts in protein aggregate stability define proteostasis decline in the aging human brain

Edward Anderton[1,2*], Jordan B. Burton[1], Christina D. King[1], Anna C. Foulger[1], Dipa Bhaumik[1], Daria Timonina[1], Zachary Mayeri[1], Manish Chamoli[1], Julie K. Andersen[1], Birgit Schilling[1], Gordon J. Lithgow[1*].

Affiliations:

1. Buck Institute for Research on Aging, 8001 Redwood Blvd., Novato, CA, 94945, USA

2. USC Leonard Davis School of Gerontology, University of Southern California, 3715 McClintock Ave, Los Angeles, CA, 90191, USA

***Corresponding Authors**

Abstract

Loss of proteostasis and the accumulation of insoluble protein aggregates are features of aging across model organisms and occur in all major age-related neurodegenerative diseases; yet how aggregation proceeds during normal human brain aging remains unknown. Here, using detergent-fractionation proteomics, we show that brain aging does not involve uniform aggregate accumulation; rather, the insoluble proteome undergoes asymmetric remodeling beginning in midlife, with maximum-stability aggregates declining sharply by old age and intermediate-stability aggregates accumulating progressively before accelerating after age 80. Intermediate-stability aggregates are prone to liquid-liquid phase separation and are enriched among Alzheimer's disease plaque and tangle constituents. Proteasome and cytosolic chaperone capacity predict individual differences in aggregate burden as strongly as chronological age, offering human-level evidence in support of therapies targeting these pathways. These findings establish aggregate remodeling as a feature of normal brain aging and position intermediate-stability aggregate accumulation as a molecular event on the path to neurodegenerative disease.

Introduction

Loss of proteostasis is a conserved hallmark of aging[1]. When proteostasis mechanisms fail, cells and tissues accumulate misfolded proteins that form insoluble protein aggregates[2]. In laboratory animal models aging is associated with the accumulation of detergent insoluble protein aggregates[3–7]. In humans, all major age-related neurodegenerative diseases involve the accumulation of detergent resistant pathological aggregates[8]. Yet, whether insoluble proteins accumulate during normal human brain aging is unknown.

Insoluble protein aggregates exist on a continuum of stability defined by their biophysical and chemical properties[9–14]. Differential detergent fractionation has been used to characterize aggregated Tau, α-synuclein, prion protein, and TMEM106B in disease contexts, exploiting the principle that detergents of different strengths isolate aggregates based on their stability state[15–18]. N-lauroylsarcosine (sarkosyl) enriches aggregates maintained by intermediate-strength interactions, whereas sodium dodecyl sulfate (SDS), a stronger denaturant, leaves only the most resistant material insoluble [14,19–22]. Sarkosyl-insoluble fractions enrich assemblies that retain biological activity such as seeding competence, which contributes to aggregate spread through tissues; SDS-resistant material, by contrast, has been associated with highly stable, sequestered deposits [20,23–28]. While the biological consequences of aggregate stability remain contested, soluble oligomers and intermediate-stability assemblies have been implicated as toxic species in neurodegeneration, in part because they retain seeding competence and can propagate through neural circuits[29,30]; whereas highly stable aggregates can limit toxicity by sequestering misfolded proteins from the functional pool[31,32]. Whether aging shifts the balance toward one stability state or another, and whether such changes overlap with disease-associated aggregation, has not been examined in the human brain.

Protein biophysical analysis established that sequence and structural features increase aggregation propensity, including β-sheet-forming segments, hydrophobicity, intrinsic

disorder, and motifs enabling multivalent interactions[33,34]. Classical amyloids such as amyloid-β aggregate through β-sheet-rich fibrillization, whereas other proteins, particularly RNA-binding proteins, assemble through liquid-liquid phase separation (LLPS) followed by maturation into solid aggregates[35–38,]. While these biophysical principles have been characterized extensively in disease contexts, whether they shape insoluble protein behavior during normal human brain aging is undetermined.

Here we asked whether normal human brain aging is characterized by the accumulation of insoluble protein aggregates. We applied parallel detergent fractionation with SDS and sarkosyl to post-mortem hippocampal tissue from disease-free females spanning the adult lifespan. Rather than uniform accumulation, we uncovered a qualitative reorganization of the insoluble proteome during aging, in which aggregates shift away from maximum-stability and towards intermediate-stability states. The proteins that accumulate possess a biophysical signature dominated by liquid-liquid phase separation propensity, rather than classical amyloid features, and are enriched among Alzheimer's disease plaque and tangle constituents.

Results

Aging induces asymmetric remodeling of detergent-insoluble proteoforms in the female brain.

We applied this parallel fractionation approach to post-mortem hippocampal tissue from disease-free females aged 20-88 years (n = 52; see Methods for inclusion-exclusion criteria). By extracting these fractions from the same tissue, we could directly compare how proteins change across stability states during female brain aging. The insoluble proteome from each fraction, and lysate (soluble + insoluble), were quantified by mass spectrometry with data-independent acquisition (DIA). For differential abundance analysis, individuals were grouped: Young (20-35 yrs), Middle (45-55 yrs), Old (65-75 yrs), and Geriatric (80-88 yrs) (Fig. 1A).

The two fractions captured largely overlapping proteins (overlap: 75-85%); however, they showed asymmetric age-related changes (Fig. 1B). The SDS-insoluble proteome showed modest decline from young to middle age but underwent fraction-wide decline in the transition to old age. In total, 82% of detected SDS-insoluble proteins decreased with age (n = 1934), representing general depletion of high-stability protein aggregates (Fig. 1C). TMEM106B, which forms bona fide amyloid fibrils in aged human brains, was a notable exception, showing significant monotonic accumulation in the SDS-insoluble fraction across the lifespan[39]. Conversely, changes in the sarkosyl-insoluble proteome were modest until the geriatric transition, after which approximately 10% of proteins (n = 303) increased significantly (Fig. 1D). Total SDS-insoluble protein burden followed a log-linear decline with age, whereas total sarkosyl-insoluble protein burden remained approximately constant (Supp. Fig 1D). Insoluble MAPT (Tau) showed concurrent depletion from SDS-insoluble aggregates alongside accumulation in sarkosyl-insoluble aggregates, though the accumulation in sarkosyl did not reach significance after FDR correction (q= 0.18) due to high variance among geriatrics (Supp. Fig. 1E). Leave-one-out analysis and covariate-adjusted models confirmed age-related changes were robust to individual subject exclusions, post-mortem interval, and biobank source; variation in effect magnitude was not associated with insoluble Amyloid Precursor Protein or Tau levels (see Methods: Robustness Estimations). Western blot analysis of a subset of samples confirmed the direction of age-related changes observed by mass spectrometry (Supp. Fig. 2A-D).

Thousands of proteins were detected in both SDS- and sarkosyl-insoluble fractions across all age groups (SDS = 2857, Sark = 3267), spanning diverse biological processes (Fig. 1B, Supp. Fig. 1A). Synaptic proteins were the most over-represented cellular component in both fractions, followed by the endomembrane system and mitochondrial proteins (Supp. Fig. 1A). Both insoluble proteomes were enriched with proteins implicated across multiple proteinopathies, including AD, PD, Huntington's disease, and prion disease (Supp. Fig. 1B). Proteins detected exclusively in the sarkosyl-insoluble fraction were enriched for mitochondrial ribosomes and ER proteins, whereas SDS-exclusive proteins showed no functional enrichment (Supp. Fig. 1C). Taken together, these data

109 indicate that aging does not drive uniform aggregate accumulation; rather, it induces
110 divergent, fraction-specific changes across the insoluble proteome including in pro-
111 aggregating, disease-associated proteins.

112 **Age-related insolubility changes are independent of expression**

113 Protein solubility is tightly coupled to expression level, and aggregation can occur when
114 proteins exceed their solubility limit[40]. The observed age-related changes in insoluble
115 protein abundance could therefore reflect altered expression rather than shifts in
116 aggregation state. To assess this, we calculated an insolubility index for each protein
117 (insoluble/lysate) and computed age-dependent slopes for insoluble abundance, lysate
118 abundance, and insolubility index separately (Fig. 1E&F). Lysate abundance was largely
119 stable with age, and pellet slopes strongly predicted index slopes in both fractions (SDS:
120 $r = 0.83$; sarkosyl: $r = 0.76$), establishing that changes in aggregate abundance rather
121 than total expression underlie observed insolubility shifts (Fig. 1E&F). Given high
122 concordance between pellet abundance and insolubility index trajectories (SDS 97.4%,
123 sarkosyl 88.5%), we chose to use pellet abundance as the measure of aggregate load
124 throughout.

125 The aging slope distributions showed a proteome-wide divergent pattern between the two
126 solubility states: 94.6% of SDS-insoluble proteins declined with age, while 66.3% of
127 sarkosyl-insoluble proteins increased (Fig. 1E&F). We hypothesized that this concurrent
128 decline and accumulation could reflect redistribution between stability states. However,
129 age-related changes were positively correlated across the proteome, and only a subset
130 of SDS-declining proteins showed significant, concurrent sarkosyl accumulation,
131 suggesting that protein is not redistributing from SDS-insoluble into sarkosyl-insoluble
132 aggregates (Supp. Fig. 3A).

133 The fraction-wide decline in SDS-insoluble abundance raised the question of whether
134 tissue composition changes, such as synapse or neuronal loss, could account for the
135 observed patterns. Synaptic and postsynaptic density proteins showed stable lysate

abundance with age while their SDS insolubility indices declined, and cell-type deconvolution confirmed that neuronal proportions were unchanged, ruling out synapse or neuronal loss as explanations (Supp. Fig. 4A, C, E). Conversely, synaptic proteins showed increases in sarkosyl insolubility index, consistent with a shift toward intermediate-stability aggregate states during aging (Supp. Fig. 4B, D).

Midlife marks the onset of progressive aggregate remodeling

To identify the temporal trajectories of insoluble proteins across the lifespan, we fitted generalized additive models to each protein's abundance as a function of age and clustered proteins with significant age effects by trajectory similarity (see Methods for filtering criteria). All age-changing SDS-insoluble proteins declined with age, most following a biphasic pattern with slight declines from young to middle age and then steep declines in the middle-to-old transition (Fig. 1G). Conversely, most age-changing sarkosyl-insoluble proteins increased modestly from young through to old age before accelerating sharply in the geriatric group (Fig. 1H). We applied a monotonic trend test to sarkosyl-insoluble proteins that accumulate during aging and found that 110 (36%) proteins reached significance after multiple testing correction (Mann-Kendall, $q < 0.05$; median $p = 0.031$), and all 303 exhibited positive trend direction, supporting that the accumulation of aggregates is a progressive process spanning decades rather than a late-life threshold event.

Selective accumulation of sarkosyl-insoluble aggregates is associated with liquid-liquid phase separation

We hypothesized that biochemical and biophysical properties might distinguish proteins that decline in SDS or selectively accumulate in sarkosyl-insoluble aggregates during aging. To assess this, we compiled a panel of established predictors of protein aggregation propensity spanning intrinsic aggregation (TANGO, Zagg)[41,42], predicted solubility (CamSol)[43], supersaturation[44], LLPS propensity (catGranule, FuzDrop)[45,46], RNA-binding capacity[47], biochemical and 3D structural properties[47], AlphaFold predicted

163 disorder[48], post-translational modification sites[47], and chaperone-mediated autophagy
164 (CMA) degradation targeting motifs[49](Fig. 2A). To benchmark these profiles, we
165 compared against 15 pro-aggregating, amyloids detectable in the hippocampus such as
166 Amyloid β, Tau, and α-synuclein.

167 We first asked whether proteins vulnerable to insolubility, independent of age, share
168 biophysical features with classical amyloids. For each protein group, we calculated
169 feature enrichment relative to the hippocampal proteome (Figure 2A). Amyloids exhibited
170 the expected aggregation signature: elevated TANGO scores, high β-sheet propensity,
171 and low predicted solubility (Fig. 2A). The detergent-insoluble proteomes, by contrast,
172 showed a largely opposite profile: lower aggregation propensity, reduced β-sheet content,
173 and higher predicted solubility than the hippocampal proteome (Fig. 2A). Rather than
174 classical aggregation features, insoluble proteins were characterized by elevated LLPS
175 propensity (catGranule) and RNA-binding capacity (Fig. 2A). The connection with LLPS
176 and RNA-binding capacity is particularly striking since many neurodegenerative disease
177 proteins such as FUS, TDP-43, α-synuclein and HNRNPA1 associate with RNA-protein
178 granules *in vivo*[38]. Beyond phase separation propensity, insoluble proteins also showed
179 elevated K48 ubiquitination and higher CMA motif density compared to the background
180 proteome, consistent with greater steady state targeting for degradation (Fig. 2A). The
181 single point of convergence between amyloids and the broader insoluble proteome was
182 high supersaturation, indicating that expression near the solubility limit is a common
183 feature of aggregation-vulnerable proteins (Fig. 2A).

184 We next asked whether proteins showing age-related changes represent biophysically
185 distinct subgroups. We performed biophysical enrichment of SDS-declining and sarkosyl-
186 accumulating proteins, comparing each group against its detection background to
187 account for baseline differences (Fig. 2B). The SDS-insoluble proteome was depleted for
188 classical aggregation features relative to the hippocampal proteome (Fig. 2A). Within this
189 depleted background, SDS-insoluble age-declining proteins showed modest relative
190 enrichment for TANGO scores, beta-sheet propensity, and hydrophobicity, indicating that

191 the proteins lost during aging are the most aggregation-prone members of their fraction
192 (Fig. 2B). However, because the SDS-insoluble proteome is itself depleted for classical
193 aggregation features, this relative enrichment does not establish a specific aggregation
194 mechanism for their decline. By contrast, the sarkosyl-insoluble age-accumulating
195 proteins were depleted of classical aggregation features but enriched for LLPS propensity
196 (catGranule and FuzDrop), consistent with condensate-mediated aggregation (Fig. 2B).
197 While both LLPS predictors were enriched among sarkosyl-accumulating proteins,
198 catGranule and FuzDrop scores were only modestly correlated (r=0.24) which is
199 consistent with their distinct training datasets. FuzDrop predicts based on entropy-driven
200 disordered interactions, whereas catGranule is a broader phase separation predictor
201 incorporating RNA-binding and structural features. Among sarkosyl-accumulating
202 proteins, 73% scored in the top tertile for at least one LLPS predictor, partitioning into two
203 approximately equal populations: proteins scoring high on catGranule but not FuzDrop
204 (36%), and proteins scoring high on both predictors (37%). These populations, therefore,
205 represent distinct routes to LLPS-driven aggregation, one mediated by entropy-based
206 disordered interactions captured by both predictors and one driven by features such as
207 multivalent interactions and RNA-binding capacity that FuzDrop does weight. Because
208 LLPS predictors correlate with sequence length, we used multivariate logistic regression
209 to confirm that both catGRANULE and FuzDrop independently distinguished
210 accumulators after controlling for sequence length, abundance, and peptide counts (see
211 Methods). Taken together, these data demonstrate that age-related sarkosyl
212 accumulation is more likely to be driven by LLPS propensity than classical amyloid
213 features, with two biophysically distinct subpopulations converging on condensate-
214 mediated aggregation.

215 **Proteins that accumulate in sarkosyl-insoluble aggregates during aging are**
216 **enriched in AD plaques and tangles.**

217 Sarkosyl is widely used to study pro-aggregating proteins in neurodegenerative disease,
218 and several studies have reported alterations to the sarkosyl-insoluble proteome in AD
219 brains[50–54]. The accumulation of sarkosyl-insoluble protein in the geriatric group, when

220 AD risk increases sharply, led us to question whether this material resembles disease-
221 associated aggregates. We compared our data against the NeuroPro database, which
222 compiles AD proteomic studies including laser microdissection of amyloid plaques and
223 neurofibrillary tangles[55].

224 We first determined fold enrichment of proteins vulnerable to insolubility, irrespective of
225 age. Both insoluble proteomes showed enrichment for plaque-associated proteins
226 compared to the hippocampal proteome, with roughly half of insoluble-detected proteins
227 appearing in the plaqueome; tangle enrichment followed a similar pattern with lower
228 absolute representation (Fig. 3A&B, Supp. Fig. 5A&B). When comparing age-changing
229 proteins in each insoluble fraction a clear dichotomy emerged. Proteins declining in the
230 SDS-resistant, maximally stable fraction during aging showed no additional enrichment
231 for plaques or tangles beyond baseline (Fig. 3A&B, Supp. Fig. 5C). Proteins accumulating
232 in the intermediate-stability sarkosyl-insoluble pool, by contrast, showed pronounced
233 enrichment for both AD plaque and tangle constituents (Fig. 3A&B, Supp. Fig. 5D). This
234 result was remarkable since it suggests that aggregate accumulation during disease-free
235 aging overlap significantly with AD.

236 We next asked whether sarkosyl-accumulating proteins have been identified as AD CSF
237 biomarker candidates, using a meta-analysis of putative biomarkers identified across at
238 least three independent discovery cohorts[56]. CSF biomarkers were enriched at baseline
239 in both detected insoluble proteomes; however, only proteins that accumulate in the
240 sarkosyl-insoluble fraction during aging showed significant enrichment above baseline,
241 extending the disease relevance of age-related sarkosyl accumulation beyond brain
242 tissue to peripheral biomarker signatures (Fig. 3A&B).

243 Fifty-eight proteins that increased in the sarkosyl-insoluble fraction with age were
244 independently detected in both amyloid plaque and neurofibrillary tangle proteomes. Most
245 of these (37/58, 64%) showed concurrent depletion from the SDS-insoluble fraction,
246 consistent with loss from maximally stable aggregates alongside accumulation in
247 intermediate-stability states (Fig. 3C). The remainder were either stable in the SDS-

248 insoluble fraction or showed a trend toward higher SDS-insoluble levels during aging.
249 These 58 proteins encompassed synaptic components spanning presynaptic machinery,
250 postsynaptic cytoskeletal markers, and four major brain 14-3-3 isoforms; proteostasis
251 machinery including SQSTM1(p62), VPS35, USP14, and cytosolic and mitochondrial
252 chaperones including HSP90AB1, HSPA4L, HSPA9, and TRAP1; mitochondrial enzymes
253 of the TCA cycle, pyruvate dehydrogenase complex, and oxidative phosphorylation; and
254 RNA-binding proteins implicated in aberrant granule formation (HNRNPA2B1,
255 HNRNPK)[57,58] (Fig. 3C).

256 **Sarkosyl-insoluble aggregates span synaptic, mitochondrial, and proteostasis**
257 **machinery in the aging female hippocampus**

258 Because aggregation depletes functional protein, we asked which biological functions are
259 represented among sarkosyl-insoluble accumulators. Functional annotation of all 303
260 accumulating proteins revealed nine broad categories (Table 1).

261 Cytoskeletal and synaptic proteins were the largest functional group, with actin
262 cytoskeleton and cell adhesion components (n = 41), postsynaptic scaffolding and
263 signaling proteins (n = 23), presynaptic machinery (n = 13), microtubule and motor
264 proteins (n = 15), all six brain 14-3-3 isoforms, and the complete neuronal dystrophin-
265 associated complex (Table 1).

266 Mitochondrial proteins were the second largest category (n = 43), including energy
267 metabolism enzymes (n = 28), proteostasis and import machinery (n = 8), and
268 mitochondrial RNA and translation factors (n = 7) (Table 1). Age-accumulating
269 mitochondrial proteins were predominantly matrix enzymes, particularly TCA cycle
270 components and quality control chaperones HSPA9 (mtHsp70) and TRAP1 (mtHsp90);
271 membrane-integrated complexes of the electron transport chain, ATP synthase, and TIM
272 translocase were, by contrast, constitutively detergent-resistant at all ages. The co-
273 aggregation of TOMM70, which coordinates substrate recognition at the outer membrane
274 import channel, alongside the matrix chaperones and enzymes it helps deliver, raises the

275 possibility that protein import represents a bottleneck at which misfolded cargo
276 accumulates (Table 1).

277 The remaining categories included membrane trafficking proteins (n = 36), among them
278 VPS35, the retromer cargo-recognition subunit linked to familial Parkinson's disease[59];
279 proteostasis machinery (n = 32) including ubiquitin-proteasome components, cytosolic
280 chaperones, and selective autophagy receptors such as SQSTM1/p62; and RNA-binding
281 and translation proteins (n = 22) (Table 1). Consistent with the LLPS and RNA-binding
282 signature identified in the biophysical analysis, this last group included mRNA processing
283 factors, translation initiation components, and aminoacyl-tRNA synthetases from both
284 cytoplasmic and mitochondrial compartments, suggesting that mitochondrial translational
285 capacity is itself vulnerable to age-related aggregation (Table 1). Taken together, the
286 proteins accumulating in sarkosyl-insoluble aggregates during aging represent core
287 machinery required for synaptic function, suggesting that proteostasis decline during
288 aging may erode synaptic activity independently of synapse loss.

289 **Proteostasis machinery is enriched in insoluble fractions**

290 The accumulation of mitochondrial quality control machinery in sarkosyl-insoluble
291 aggregates during aging led us to question whether proteostasis machineries were
292 enriched in either fraction. Their presence could provide clues as to which machineries
293 handle the different aggregate species, and which could be vulnerable to co-aggregation
294 during aging. To test this, we calculated composite abundance signatures for nine
295 proteostasis network branches using the proteostasis network consortium database
296 annotations[60,61]. Autophagy machinery and cytosolic chaperones were significantly
297 enriched in both insoluble fractions across all ages (Supp. Fig. 6A). Most proteostasis
298 machineries were present in aggregates but remained stable across the lifespan (Supp.
299 Fig. 6A). Autophagy and cytosolic chaperone proteins were enriched in both insoluble
300 fractions irrespective of age, indicating that these machineries constitutively co-
301 fractionate with aggregates (Supp. Fig. 6A). The two fractions diverged, however, with
302 respect to age-related changes: autophagy components were enriched among SDS-

303 declining proteins but depleted from sarkosyl-insoluble accumulators (Supp. Fig. 6A).
304 This asymmetry is consistent with a model in which autophagy actively clears SDS-
305 resistant aggregates and declines alongside them, while sarkosyl-insoluble material
306 accumulates through a pathway that autophagy does not effectively engage.
307 Mitochondrial protein homeostasis showed a trend towards enrichment in the sarkosyl
308 age-changing insoluble proteome consistent with the enrichment of mitochondrial
309 proteins in that fraction (Fig. 4, Supp. Fig. 6A).

310 We applied the same approach to CNS cell types using published composite cell type
311 marker data[62]. Neuronal proteins were enriched in both insoluble fractions, microglial
312 proteins were depleted across both, while astrocyte markers trended toward enrichment
313 among sarkosyl-insoluble accumulators (Supp. Fig. 6B). This pattern indicates that the
314 insoluble proteome is neuronally dominated at all ages but that astrocytic proteins may
315 be selectively vulnerable to age-related accumulation while microglial proteins are largely
316 excluded.

317 **Proteostasis network capacity predicts hippocampal aggregate burden**
318 **independently of chronological age**

319 While aging has a significant effect on insoluble protein levels, aggregate burden was
320 highly heterogeneous even among age-matched individuals (Supp. Fig. 1D), suggesting
321 that other factors contribute to aggregate load. We hypothesized that proteostasis
322 network capacity could explain inter-individual variation and built linear models predicting
323 insoluble protein burden using lysate abundance of nine proteostasis network branches,
324 controlling for age as a covariate.

325 Two pathways showed significant protective associations with sarkosyl-insoluble
326 accumulation: proteasome capacity yielded the largest individual effect size, followed by
327 cytosolic chaperones. We applied the same approach to cell-type signatures and found
328 that microglia showed a protective association with sarkosyl-insoluble burden consistent
329 with literature implicating microglia in aggregate clearance in the CNS[63] (Fig. 5B).

330 Mitochondrial proteostasis capacity, by contrast, showed a positive association with
331 insoluble burden in both fractions (Fig. 5A). We ruled out mitochondrial mass as a
332 predictor using total mitochondrial protein signal as a proxy, indicating that the association
333 is specific to proteostasis capacity rather than organelle abundance. Autophagy and ER
334 proteostasis showed significant positive associations with SDS-insoluble burden; ER also
335 showed a trend for sarkosyl and translation showed positive trends in both fractions (Fig.
336 5A). The positive direction of these biosynthesis and import-associated pathways
337 contrasted with the protective direction of clearance mechanisms, suggesting that protein
338 production and import track with aggregate load while degradation capacity limits it.

339 The translation category encompassed hundreds of functionally heterogeneous proteins
340 and so we decomposed it into bona fide translation machinery and co-translational
341 proteostasis proteins (Supp. Fig. 6C). Consistent with the broader pattern, abundance of
342 mitochondrial and cytosolic ribosomes was positively associated with insoluble protein
343 levels across both fractions (Supp. Fig. 6C). Mitochondrial ribosome biogenesis was
344 specifically associated with sarkosyl-insoluble accumulation, and mitochondrial protein
345 import machinery was positively associated with insoluble protein across both fractions
346 (Supp. Fig. 6C). Conversely, cytosolic elongation and termination factors and ribosome-
347 associated nascent chain chaperones (NAC/RAC complex) both displayed protective
348 associations, implicating co-translational proteostasis as a determinant of aggregate load
349 (Supp. Fig. 6C). Taken together, these data indicate that aggregate burden in human
350 brain reflects a balance between protein production and clearance capacity, with
351 proteasome, cytosolic chaperones, and co-translational quality control limiting
352 accumulation while biosynthetic and import pathways track with load.

353 **Discussion**

354 Our proteome-wide analysis reveals that human brain aging does not drive uniform
355 aggregate accumulation; rather, the insoluble proteome undergoes qualitative
356 remodeling, with maximally stable SDS-resistant aggregates declining while
357 intermediate-stability sarkosyl-insoluble proteins accumulate progressively before

358 accelerating after age 80. Sarkosyl-accumulating proteins possess a biophysical
359 signature centered on LLPS propensity rather than classical amyloid features; however,
360 accumulating proteins show strong enrichment among AD plaque and tangle
361 constituents. Aggregate burden varied substantially among age-matched individuals,
362 with proteostasis network capacity explaining as much variance as chronological age,
363 implying that aggregate accumulation is not an inevitable feature of aging. Because the
364 proteins suppressed by high proteostasis capacity are the same proteins enriched in AD
365 pathology, individual differences in clearance capacity may influence accumulation of
366 disease-relevant aggregates during normal aging.

367 The temporal separation of these changes implies that SDS decline and sarkosyl
368 accumulation are independent remodeling events rather than sequential phases of a
369 single process. SDS-insoluble aggregates decline most dramatically during the middle-
370 to-old transition, whereas sarkosyl-insoluble accumulation remains gradual until the
371 geriatric transition, when it accelerates markedly. The net effect is a shift in the aggregate
372 landscape away from sequestered, maximally stable deposits and toward labile,
373 intermediate-stability material associated with seeding competence in disease contexts.
374 The surge in sarkosyl-insoluble aggregates at the geriatric transition may represent a
375 threshold phenomenon in which clearance mechanisms become overwhelmed, though
376 our cross-sectional design cannot test this directly. AD-associated pathology develops
377 biochemically for decades before cognitive symptoms manifest[64], and it is the AD-
378 enriched sarkosyl-insoluble fraction that accelerates in the ninth decade when AD
379 incidence rises sharply.

380 The proteome-wide decline of SDS-insoluble aggregates was unexpected given that
381 aging in *C. elegans* and mice is associated with SDS-insoluble accumulation[4,65,66]. One
382 possible interpretation is that maximally stable aggregates represent protective detention
383 structures like aggregsomes. Indeed, sequestration of soluble Aβ oligomers and HTT
384 peptides into insoluble deposits reduces toxicity[32,67]. However, the SDS-insoluble
385 proteome lacked classical aggresome markers: HDAC6[68] was not detected, and
386 SQSTM1/p62[69] and BAG3[70] appeared exclusively in sarkosyl-insoluble material. An

387 alternative interpretation is that the SDS-insoluble fraction we measure represents a
388 snapshot of material passing through autophagy and the age-related decline in SDS
389 insoluble material reflects reduced flux. This is supported by the fact that autophagy
390 components are enriched among age-declining SDS-insoluble proteins, and autophagy
391 pathway expression tracks positively with SDS-insoluble burden. These models are not
392 mutually exclusive because sequestered aggregates should be targeted to autophagy.
393 Whether SDS-insoluble material in the human brain serves a protective function,
394 represents a clearance intermediate, or both, remains to be determined.

395 Sarkosyl-accumulating proteins possess a biophysical signature distinct from classical
396 amyloids. Rather than elevated beta-sheet propensity and hydrophobicity, they are
397 characterized by greater sequence length, high LLPS propensity across two orthogonal
398 predictors, and higher predicted solubility. LLPS proceeds through weak multivalent
399 interactions largely independent of surface hydrophobicity, and sequence length
400 correlates with multivalency[71]. The LLPS predictor profiles for accumulators partition into
401 two populations, suggesting distinct biophysical routes converging on condensate
402 formation. RNA-binding proteins constitute the largest functional category among
403 accumulators; however, RNA-binding capacity is not enriched above the sarkosyl-
404 detected background, suggesting that LLPS-driven aggregation must proceed through
405 broader mechanisms not restricted to canonical RNA-protein interactions. The
406 enrichment of LLPS-prone proteins among AD plaque and tangle constituents suggests
407 that phase separation may represent a pathway to pathological aggregation operating
408 alongside classical amyloid formation. It has been proposed that condensates can mature
409 into solid aggregates over time[38], providing a plausible route from phase separation to
410 detergent-insoluble material during aging, although the mechanism for solidification is
411 unknown.

412 Aggregate burden was highly heterogeneous among age-matched individuals, and
413 proteostasis network machinery abundance explained substantial inter-individual
414 variance. Proteasome and cytosolic chaperone abundance showed negative, protective
415 associations with sarkosyl-insoluble burden, whereas biosynthetic and import pathways

416 showed positive associations with aggregate load. When combined in a linear model
417 proteostasis predictors tripled the variance explained by age alone, predicting almost 40%
418 of total variance in insoluble burden. Contrary to expectation, autophagy network
419 abundance was not protective against sarkosyl-insoluble accumulation. Moreover,
420 autophagy components were depleted among sarkosyl accumulators but enriched among
421 age-declining SDS-insoluble proteins, suggesting that autophagy preferentially interacts
422 with SDS-insoluble material. The protective association of proteasome capacity aligns
423 well with model organism studies which implicate UPS decline as a driver of age-related
424 aggregation[72]. Given that the proteins suppressed by high proteasome capacity are
425 strongly enriched among AD plaque and tangle constituents, these data provide human-
426 level evidence that UPS capacity may influence disease-relevant aggregate
427 accumulation.

428 Mitochondrial proteostasis is emerging as a conserved age-related vulnerability, with
429 mitochondrial protein aggregation now documented across *C. elegans*, mouse, and now
430 human brain[3–5,66,73]. Mitochondrial proteins were prominent were prominent in the
431 insoluble proteome but only matrix enzymes and quality control machinery showed age-
432 related accumulation; membrane-integrated ETC complexes, ATP synthase, and TIM
433 translocase were insoluble at all ages. One possible explanation for mitochondrial protein
434 vulnerability is precursor over-accumulation stress (mPOS): when mitochondrial import
435 capacity declines due to mitochondrial dysfunction, nuclear-encoded mitochondrial
436 proteins accumulate in the cytosol, where they are prone to aggregation[74]. In this context,
437 the link we observe between mitoribosome biogenesis factor abundance and overall
438 sarkosyl-insoluble burden makes sense since biogenesis demand necessarily correlates
439 with the pool of import-dependent precursors vulnerable accumulation in the cytosol. This
440 model implies a feedforward loop in which mitochondrial dysfunction and mitochondrial
441 protein aggregation reinforce one another, whether aggregation occurs in the cytosol
442 following failed import or within the matrix itself.

443 This study has limitations worth acknowledging. Our cohort consisted exclusively of
444 females, selected for their higher lifetime AD risk[75] and whether males show equivalent

aggregation patterns should be addressed in future work. While subjects were screened for neurodegenerative disease by neuropathological examination, we cannot exclude subcellular pathology, and variance in insoluble amyloid and tau among the oldest old may partly reflect preclinical heterogeneity. All subjects were cognitively normal at death, but we lack longitudinal cognitive data and cannot assess the functional relevance of insoluble protein changes. Our biophysical analysis was based on sequence-level predictors; we did not perform ultrastructural or material-state validation, so assignments of LLPS behavior remain to be demonstrated experimentally. Future work should prioritize biochemical characterization, expansion to male cohorts, and validation in murine models.

This study establishes that disease-free human brain aging is characterized by qualitative remodeling of the insoluble proteome rather than uniform aggregate accumulation, with maximally stable and intermediate-stability aggregate pools showing independent and opposing trajectories. The proteins that accumulate in intermediate-stability aggregates during normal aging are the same proteins enriched in AD plaques and tangles, and their accumulation is constrained by proteostasis capacity, particularly proteasome and cytosolic chaperone abundance. These observations provide human-level evidence that the molecular events linking normal aging to neurodegenerative disease are potential targets for intervention before clinical symptoms emerge.

465 **Methods**

466 All statistical tests were performed using R base package unless otherwise stated.

467 **Human brain tissue sourcing**

468 Human brain samples were sourced from the NIH Neurobiobank consortium, which
469 encompasses several biobanks across the contiguous United States. Biobanks follow the
470 same standardized sample processing and handling procedures.

471 **Subject inclusion / exclusion criteria**

472 Frozen post-mortem human coronal tissue sections encompassing the entire
473 hippocampal formation from the level of the lateral geniculate nucleus were obtained from
474 58 female donors aged 20-88 years (median post-mortem interval: 17 hours; IQR: 14-23
475 hours). Females were chosen due to their increased lifetime risk of neurodegeneration,
476 in particular AD[76]. All hippocampus samples were deemed disease free by expert
477 neuropathologists. To isolate the effects of normal aging on protein aggregation from
478 confounding disease processes, we applied stringent exclusion criteria. Donors with a
479 clinical history of neurodegenerative disease (Alzheimer's disease, Parkinson's disease,
480 dementia), cerebrovascular events (stroke, transient ischaemic attack), psychiatric
481 disorders (depression, anxiety, bipolar disorder, schizophrenia), substance abuse, or
482 smoking were excluded. We further excluded donors with systemic inflammatory or
483 autoimmune conditions (rheumatoid arthritis, autoimmune disorders, hepatitis A/B/C),
484 organ or bone marrow transplant recipients, and those with major organ disease including
485 cardiovascular disease (myocardial infarction, coronary artery disease, congestive heart
486 failure, cardiomyopathy), chronic pulmonary disease (emphysema, COPD, pulmonary
487 fibrosis, sleep apnoea), gastrointestinal disease (coeliac disease, Crohn's disease),
488 hepatic disease (cirrhosis, NAFLD/NASH), chronic kidney disease, diabetes, and macular
489 degeneration. A subset of common conditions was included: asthma, osteoarthritis,
490 fibromyalgia, endometriosis, IBS, GERD, Barrett's oesophagus, glaucoma, cataracts,
491 venous thromboembolism, kidney stones, and non-CNS cancers without brain

492 metastases. Hypertension and hypercholesterolaemia were included due to the very high
493 overall prevalence amongst the elderly[77].

494 **Brain tissue homogenization**

495 Homogenization and processing of the lysates was completed following universal
496 precautions in a BSL2 certified tissue culture hood. A segment of hippocampal tissue
497 encompassing all regions of the hippocampal formation was submerged in 150 μL of lysis
498 buffer containing protease, phosphatase and deacylase inhibitors (20 mM Tris base, pH
499 7.4, 100 mM NaCl, 1 mM $MgCl_2$, 30 mM NAD, 5 mM Trichostatin A) per mg of frozen
500 tissue in a pre-cooled 7 mL Dounce homogenizer, on ice. To homogenize the tissue, 30
501 strokes were applied with pestle A, followed by 30 strokes with pestle B. Homogenate
502 was removed into a pre-cooled 15 mL conical tube and sonicated in a 4°C water bath
503 using the Bioruptor for 5 cycles of 30 seconds on and 60 seconds off at medium intensity.
504 To remove cell debris, the lysate was centrifuged in a pre-cooled, 4°C swinging bucket
505 centrifuge at 3000×g for 4 minutes. The supernatant (lysate) was removed and stored at
506 -80°C until subsequent processing. The pellet was discarded.

507 **Insoluble protein isolation**

508 Samples were processed in batches of eight and, to minimize batch processing effects,
509 an equal number of subjects from each of the pre-defined age groupings were processed
510 in each batch. Subjects were selected randomly for each batch. The lysate protein
511 concentration was quantified by BCA according to manufacturer's instructions. To
512 normalize input for insoluble protein isolation, an aliquot of lysate equivalent to 2 mg of
513 total protein was added to a sterile, ice-cold Eppendorf tube and the volume was
514 equalized across all samples by addition of ice-cold lysis buffer containing protease,
515 phosphatase inhibitor and deacylase inhibitor (20 mM Tris base, pH 7.4, 100 mM NaCl,
516 1 mM MgCl2, 30mM NAD, 5mM Trichostatin A), typically to 1.2 mL. The protein solution
517 was centrifuged in a 4°C pre-cooled benchtop centrifuge at 20,000×g for 15 minutes to
518 pellet aqueous-insoluble proteins. The supernatant was collected as the aqueous-soluble
519 fraction and stored at -80°C. The insoluble pellet was incubated in 1 mL of 1% (w/v) SDS

520 or 1% (w/v) sarkosyl lysis buffer containing protease and phosphatase inhibitor ((20 mM
521 Tris base, pH 7.4, 100 mM NaCl, 1 mM MgCl2, 30mM NAD, 5mM Trichostatin A)
522 overnight at room temperature. The pellet was then vortexed vigorously to dissolve. Each
523 sample was vortexed for the same time and intensity. The solution was checked every
524 minute by stereoscopic microscope to determine if the pellet had fully dissolved. A cutoff
525 of 10 cycles of 1-minute vortexing was applied to define empirically the maximum amount
526 of vortexing. The sample was centrifuged at room temperature at 20,000×g for 15 minutes
527 to pellet detergent-insoluble proteins. The supernatant was collected as the 1% SDS or
528 1% sarkosyl soluble fraction. The remaining insoluble pellet was resuspended in 1 mL of
529 1% SDS or 1% sarkosyl lysis buffer and solubilized by vigorous vortexing using the same
530 cutoffs. This was repeated until the third detergent-soluble fraction had been collected.
531 The remaining pellet we define as the 1% SDS or 1% sarkosyl insoluble protein fraction.
532 To redissolve the final pellet, 60 μL of 70% (v/v) formic acid was added before sonication
533 in a Bioruptor at maximum intensity without cooling for 10 cycles of 1 minute on and 30
534 seconds off. This was followed by probe sonication at 70% intensity for 2 cycles of 20
535 seconds. The sample was then dried using a SpeedVac at maximum spin speed at 45°C.
536 The resulting dried pellet was resolubilized in 2× LDS gel loading buffer with 5% (v/v)
537 beta-mercaptoethanol and sonication in the Bioruptor for 5 cycles of 30 seconds on and
538 30 seconds off at maximum intensity. Samples were then boiled at 90°C for 10 minutes
539 before storage at -20°C. The sample containing an unknown quantity of insoluble protein
540 was then processed for mass spectrometry. An aliquot of the lysate (input) equivalent to
541 300 μg was processed by mass spectrometry in parallel.

542 **Mass Spectrometry Methods**

543 **Proteolytic Digestion**

544 The tissue homogenate or insoluble fraction was resuspended in 100 μL of 4% SDS in
545 50 mM triethylammonium bicarbonate buffer (TEAB) through vigorous mixing and
546 incubated at 90°C for 1 hour. Samples were treated with 20 mM dithiothreitol in 50 mM
547 TEAB at pH 7 at 56°C for 10 minutes, cooled to room temperature for an additional 10

548 minutes, and alkylated with 40 mM iodoacetamide in 50 mM TEAB (pH 7) at room
549 temperature for 30 minutes in the dark. The samples were acidified by adding 6.5 μL of
550 12% phosphoric acid, and a fine precipitate formed after addition of 500 μL S-trap buffer
551 and mixing by inversion. The entire mixture was added to S-trap spin columns (Protifi)
552 and centrifuged at 4,000×g for 20 seconds or until fully eluted, followed by a wash with
553 400 μL of S-trap buffer. Samples were incubated with sequencing-grade trypsin
554 (Promega) dissolved in 50 mM TEAB (pH 7) at a 1:25 enzyme:protein ratio for 1 hour at
555 47°C; additional trypsin was added at the same ratio and digestion proceeded at 37°C
556 overnight. Peptides were eluted from the S-trap columns and dried by centrifugal
557 evaporation, then resuspended in 800 μL of 1% formic acid in water and desalted using
558 10 mg Oasis SPE cartridges (Waters) for the lysate or ZipTips for the insoluble fractions.
559 Desalted elutions were dried by centrifugal evaporation and resuspended in 20 μL of 0.2%
560 formic acid in water for the insoluble fractions and in 100 μL of 0.2% formic acid in water
561 for the lysate. Indexed Retention Time Standards (iRT, Biognosys) were added to each
562 sample according to the manufacturer's instructions.

563 **Chromatographic Separation and Mass Spectrometric Analysis**

564 SDS-insoluble fractions and lysates were acquired on a Waters M-Class HPLC coupled
565 to a ZenoTOF 7600 mass spectrometer (SCIEX) with an OptiFlow Turbo V Ion Source.
566 The solvent system consisted of 0.1% formic acid in water (solvent A) and 99.9%
567 acetonitrile, 0.1% formic acid in water (solvent B). Digested peptides were loaded onto a
568 Luna Micro C18 trap column (20 × 0.30 mm, 5 μm particle size; Phenomenex) over 2
569 minutes at 10 μL/min using 100% solvent A, and eluted onto a Kinetex XB-C18 analytical
570 column (150 × 0.30 mm, 2.6 μm particle size; Phenomenex) at 5 μL/min. Insoluble
571 fractions were separated using a 45-minute linear gradient from 5 to 32% B, followed by
572 an increase to 80% B for 1 minute, a hold at 80% B for 2 minutes, a decrease to 5% B for
573 1 minute, and a hold at 5% B for 6 minutes (55 minutes total acquisition time). Lysates
574 were separated using a 120-minute linear gradient from 5 to 32% B with the same wash
575 and re-equilibration steps (130 minutes total). For both, 4 μL of digested peptides were

576 loaded. Ion source parameters were: gas 1 at 10 psi, gas 2 at 25 psi, curtain gas at 30
577 psi, CAD gas at 7 psi, source temperature 200°C, column temperature 30°C, positive
578 polarity, spray voltage 5000 V. Data-independent acquisition (SWATH-DIA) was
579 performed with survey MS1 spectra acquired over 395-1005 Da (accumulation time 100
580 ms, declustering potential 80 V, collision energy 10 V), with time bins to sum set to 8 and
581 all channels enabled. MS2 spectra were collected over the same range using 80 variable
582 windows (accumulation time 25 ms, dynamic collision energy, charge state 2, Zeno
583 pulsing enabled). Total cycle time was 2.5 seconds.

584 Sarkosyl-insoluble fractions were acquired on a Dionex UltiMate 3000 system coupled to
585 an Orbitrap Exploris 480 mass spectrometer (Thermo Fisher Scientific). The solvent
586 system consisted of 2% acetonitrile, 0.1% formic acid in water (solvent A) and 80%
587 acetonitrile, 0.1% formic acid (solvent B). Digested peptides (1:5 dilution) were loaded
588 onto an Acclaim PepMap 100 C18 trap column (0.1 × 20 mm, 5 μm particle size; Thermo
589 Fisher Scientific) over 5 minutes at 5 μL/min with 100% solvent A, and eluted onto an
590 Acclaim PepMap 100 C18 analytical column (75 μm × 50 cm, 3 μm particle size; Thermo
591 Fisher Scientific) at 300 nL/min using the following gradient: 2.5 to 24.5% B over 125
592 minutes, 24.5 to 39.2% B over 40 minutes, up to 98% B in 1 minute, and back to 2.5% B
593 in 1 minute, with 30 minutes re-equilibration (210 minutes total). Each sample was
594 acquired in data-independent acquisition (DIA) mode[78–80]. Full MS spectra were collected
595 at 120,000 resolution (AGC target 3×10^6 ions, maximum injection time 60 ms, 350-1,650
596 m/z) and MS2 spectra at 30,000 resolution (AGC target 3×10^6 ions, automatic injection
597 time, NCE 30, fixed first mass 200 m/z). The DIA isolation scheme consisted of 26
598 variable windows covering 350-1,650 m/z with 1 m/z overlap[79].

599 **DIA-MS Data Processing, Quantification, and Statistical Analysis**

600 Because SDS- and sarkosyl-insoluble fractions were acquired on independent
601 instruments with distinct DIA schemes, all quantitative analyses were performed within
602 acquisition runs; age-dependent fold changes were calculated independently for each
603 detergent condition and were not compared in absolute magnitude across fractions.

604 SDS-insoluble and lysate data were analyzed using Spectronaut (version
605 17.6.230428.55965; Biognosys). The lysate was searched against the *H. sapiens*
606 panhuman spectral library (PMID: 25977788, UniProt) with 20,526 entries (accessed
607 08/28/2015); the SDS-insoluble fraction was searched using the DirectDIA algorithm
608 against the Human Reference Proteome (reviewed proteins only, UniProt) with 20,388
609 entries (accessed 07/31/2021). Sarkosyl-insoluble data were analyzed using Spectronaut
610 (version 19.4.241104.62635; Biognosys) with DirectDIA against the *Homo sapiens*
611 reference proteome with 20,411 entries (UniProtKB-SwissProt, accessed 10/06/2023).

612 For all searches, dynamic data extraction parameters and precision iRT calibration with
613 local (SDS) or non-linear (sarkosyl) regression were used. Trypsin/P was specified as the
614 digestion enzyme, allowing for specific cleavages and up to two missed cleavages.
615 Methionine oxidation and protein N-terminus acetylation were set as dynamic
616 modifications, while carbamidomethylation of cysteine was set as a static modification.
617 Protein identification at the group level required at least 2 unique peptide identifications
618 and was performed using a 1% q-value cutoff for both precursor ion and protein levels.
619 Quantification was based on the peak areas of extracted ion chromatograms (XICs) of 3-
620 6 MS2 fragment ions, specifically b- and y-ions, with 1% q-value data filtering applied. For
621 lysate data, cross-run normalization (SDS acquisition) or local normalization (sarkosyl
622 acquisition) was applied; insoluble fraction data were not normalized, to avoid bias driven
623 by differences in total protein quantity across samples. Relative protein abundance
624 changes were compared using paired t-tests with p-values corrected for multiple testing
625 using the Storey method[81] with group-wise testing corrections. Proteins with at least two
626 unique peptides, $q < 0.05$, and $|\log_2(\text{fold change})| > 0.58$ were considered significantly
627 altered.

628

629

630

631 **Data Availability**

632 Raw data and complete MS data sets have been uploaded to the Mass Spectrometry
633 Interactive Virtual Environment (MassIVE) repository, developed by the Center for
634 Computational Mass Spectrometry at the University of California San Diego, and can be
635 downloaded using the following link: (MassIVE ID number: ProteomeXchange ID:

636 **Western Blotting**

637 To validate mass spectrometry findings, western blotting was performed on SDS-
638 insoluble and sarcosyl-insoluble pellet fractions from a subset of the same cohort used
639 for proteomic analysis. Pellet fractions were resuspended in 2xLDS buffer and boiled for
640 10 minutes, before equal volumes were loaded onto 4-12% Bis-Tris gels and resolved by
641 SDS-PAGE. Proteins were then transferred to nitrocellulose membranes via semi-dry
642 transfer using a Biorad transblot turbo. Membranes were blocked in 5% non-fat milk in
643 TBS-T for 1 hour at room temperature, then incubated overnight at 4°C on a rocker with
644 primary antibodies against PIN1 (mouse monoclonal, 1:2000, Cat. No. 68127-1-Ig,
645 Proteintech), Cystatin C (CST3 rabbit polyclonal, 1:6000, Cat. No. 12245-1-AP,
646 Proteintech), total tau (Tau5, mouse monoclonal, 1:500, Cat. No. AHB0042, Invitrogen),
647 and HTT (rabbit polyclonal, N-terminal, 1:150, Cat. No. H7540, Sigma-Aldrich). Following
648 primary antibody incubation, membranes were washed in TBS-T and incubated with
649 HRP-conjugated secondary antibodies (anti-mouse or anti-rabbit as appropriate; 1:2000
650 dilution) for 2 hours at room temperature. Protein bands were visualised using Thermo
651 Scientific SuperSignal West Pico kit and imaged on a Bio-Rad ChemiDoc system. Band
652 intensities were quantified by densitometry using FIJI (ImageJ). As equal volumes rather
653 than equal protein concentrations were loaded per fraction, band intensities were not
654 normalized to a loading control; this approach preserved the native protein yield
655 differences between samples, consistent with the approach applied to the mass
656 spectrometry data.

657

Computational Methods

Dimensionality Reduction

PLS-DA dimensionality reduction analysis was performed using the mixOmics package in R.

Functional Enrichment Analysis

All functional enrichment analysis was performed using the gProfiler web server[82]. For GO and pathway enrichment analyses, the applicable experimentally measured background universe was incorporated, and the Benjamini-Hochberg method was used with an FDR correction threshold of 5%.

Protein Trajectory Modeling and Clustering

To characterize age-related changes in protein abundance and insolubility, we fitted three regression models to each protein: linear regression (abundance ~ age), natural cubic spline regression (df = 3), and generalized additive models (GAM with penalized thin-plate spline, k = 10-15, REML optimization). For each protein, abundance values were first z-scored within protein to enable cross-protein comparison.

Model performance was assessed using adjusted R^2 (linear, spline) or deviance explained (GAM), root mean square error (RMSE), and smooth term p-value. The best-fitting model was selected as that with highest adjusted R^2/deviance explained. Technical variability was quantified as the coefficient of variation (CV) of raw abundance across individuals. Proteins were filtered for trajectory clustering based on quantile thresholds applied to model fit metrics: adjusted $R^2 > 75$th percentile, RMSE < 75th percentile, CV $>$ 25th percentile (to retain dynamically changing proteins), and $p < 0.05$. These thresholds were calculated separately for each fraction (lysate, SDS-insoluble, sarkosyl-insoluble) and for aggregation ratio (insoluble/lysate) analyses. Filtered proteins were clustered by k-means (k = 6, seed = 42) based on mean z-scored values within discrete age groups: Young (20-35 yrs), Middle (45-55 yrs), Old (65-75 yrs), and Geriatric (80-88 yrs).

684 **Robustness Estimations**

685 Leave-one-out (LOO) analysis was performed to assess sensitivity of age-related
686 changes to individual subjects. For each fraction, we iteratively excluded each geriatric
687 subject (n = 14 for SDS, n = 11 for sarkosyl) and recalculated the median log2 fold change
688 (Geriatric vs Young) across all detected proteins. Robustness was evaluated using sign
689 consistency, signal-to-noise ratio, coefficient of variation, and 95% confidence intervals
690 derived from the LOO distribution. To test whether influential subjects showed evidence
691 of preclinical AD pathology, we calculated Pearson correlations between LOO influence
692 and sarkosyl-insoluble abundance of APP and MAPT.

693 Because biobank source and age group were partially confounded in this cohort, with
694 younger subjects drawn predominantly from one consortium site and older subjects from
695 another, we did not include biobank as a covariate. Post-mortem interval, the primary
696 technical variable associated with tissue banking, was modeled directly. We fitted per-
697 protein linear models (log2 abundance ~ age group + PMI) for all proteins reaching
698 significance in the primary analysis ($q < 0.05$, Geriatric vs Young) and compared the sign
699 of the covariate-adjusted Geriatric-versus-Young coefficient to the original log2 fold
700 change. PMI reached nominal significance ($p < 0.05$) for 3.7% and 0.6% of SDS and
701 sarkosyl proteins respectively. Within age groups represented by multiple biobank sites,
702 abundance profiles were highly correlated across sites for both the full detected proteome
703 and age-changing proteins (r = 0.94-0.97), indicating that site of origin does not introduce
704 systematic bias. We further tested whether age effects were reproducible within individual
705 biobank sites by comparing mean log2 abundance between adjacent age groups within
706 Maryland (Young vs Middle) and Harvard (Old vs Geriatric); 93.5% of significant sarkosyl-
707 accumulating proteins increased from Old to Geriatric within Harvard subjects and 90.1%
708 increased from Young to Middle within Maryland subjects.

709 **Cell Composition Analysis**

710 Cell proportion estimation was performed using the BrainDeconvShiny App website,
711 which uses the dTangle algorithm to estimate brain cell proportions based on published

712 single cell/nuclei datasets[83]. We used the consensus reference panel 'MultiBrain,' which
713 brings together five independent studies characterizing brain cell expression profiles, to
714 estimate cell proportions based on lysate protein abundance data[83]. dTangle achieved a
715 goodness of fit of approximately 0.4.

716 **Biophysical Feature Enrichment Analysis**

717 Proteins were annotated with biophysical and post-translational modification features.
718 Continuous features included: intrinsic disorder content (AlphaFold-derived percent
719 disorder[48]), classical aggregation propensity (TANGO score, Zagg [41,42]), supersaturation
720 (taken from[44]), LLPS propensity (catGRANULE, FuzDrop [45,46]), and predicted solubility
721 (CamSol variant score[43]). Sequence length, isoelectric point (pI), hydrophobicity
722 (GRAVY), and secondary structure propensities (helix, sheet, turn) were taken from
723 UniProt[47]. Categorical features included: RNA-binding capacity (Gene Ontology),
724 chaperone-mediated autophagy (CMA) targeting motif presence [49], ubiquitination site type
725 (K48, K63), phosphorylation, and glycosylation status were taken from Uniprot[47].

726 For continuous features, group distributions were compared using Wilcoxon rank-sum
727 tests. Categorical features were compared using Fisher's exact tests. For each feature,
728 z-scores were calculated to standardize effect sizes across continuous and categorical
729 feature types. Therefore, for continuous features, the z-score was defined as the
730 difference between the group mean and the reference mean, divided by the reference
731 standard deviation, and for categorical features, the z-score was defined as the difference
732 in proportions, standardized by the expected binomial variation of the reference
733 proportion. P-values were corrected for multiple testing within each comparison group
734 using Benjamini-Hochberg FDR correction

735 **Multivariate analysis of biophysical predictors**

736 To test whether LLPS predictor enrichment among sarkosyl-accumulating proteins could
737 be explained by correlated features such as sequence length, we performed logistic
738 regression with accumulator status as the outcome variable. The background population

consisted of all proteins detected in the sarkosyl-insoluble fraction (n = 2,208 with complete feature annotations). Accumulators were defined as proteins showing significant increase in the Geriatric versus Young comparison ($q < 0.05$, $\log_2$ fold change > 0.58; n = 245 in the model). We first fitted a detection-only model including sequence length, lysate abundance, and unique peptide counts as predictors. We then fitted a full model adding LLPS propensity scores (catGRANULE, FuzDrop). All continuous predictors were z-scored prior to model fitting. Sequence length, which showed marginal association with accumulation in the detection-only model ($p = 0.074$), was no longer significant after including LLPS predictors ($p = 0.74$). Both catGRANULE and FuzDrop remained significant after controlling for sequence length, abundance, and peptide counts ($p = 0.042$ and $p = 0.0005$, respectively). Likelihood ratio testing confirmed that LLPS predictors significantly improved the model ($p = 3.6 \times 10^{-5}$).

Alzheimer's Disease Pathology Enrichment

AD-associated proteins were obtained from the NeuroPro database, which has plaqueome and tangleome protein sets[55]. CSF biomarkers were proteins taken from a meta-analysis of CSF biomarkers and filtered to those from at least three independent studies[56]. Overlap between each insoluble proteome and the AD proteomes was quantified using Fisher's exact tests, with fold enrichment calculated relative to the hippocampal proteome to visualize baseline enrichment and aging-specific incremental enrichment. All p values were adjusted using the Benjamini-Hochberg FDR method. Venn/Euler diagrams were generated using the eulerr package in R to visualize set relationships.

Enrichment of proteostasis network and cell type-specific proteins in the insoluble proteome

We used Fisher's exact tests to assess whether proteins from specific proteostasis network (PN) branches or cell types were over-represented among (i) proteins detected in each insoluble fraction relative to the lysate-detected proteome, and (ii) age-changing proteins within each fraction relative to all detected proteins in that fraction. PN

767 annotations were obtained from the Proteostasis Network Consortium database[60,61] and
768 restricted to proteins with exclusive single-branch membership across nine branches
769 (mitochondrial, autophagy, translation, ER, cytosolic chaperones, lysosomal,
770 proteasome/UPS, extracellular, nuclear). Cell type markers for six brain cell types were
771 obtained from the BRETIGEA R package[62].

772 **Proteostasis network and cell type predictors of insoluble protein burden**

773 Two per-individual outcome variables were defined: summed log10-transformed
774 abundance of age-decreasing SDS-insoluble proteins and age-increasing sarkosyl-
775 insoluble proteins ($q < 0.05$, $|\log2FC| > 0.58$, Geriatric vs Young). For each PN branch
776 and cell type, a per-individual signature score was calculated as the mean z-scored
777 lysate abundance of all detected branch members. Each score was tested in a linear
778 model adjusting for age. BRETIGEA cell type signatures were tested using the same
779 framework. To distinguish mitochondrial proteostasis capacity from overall mitochondrial
780 abundance, total mitochondrial protein content was estimated using the annotations
781 from MitoCarta 3.0[84] and tested as an alternative predictor.

782 The translation branch was decomposed into eight mutually exclusive subcategories by
783 function and compartment: cytosolic and mitochondrial ribosomal proteins, cytosolic
784 initiation factors, cytosolic elongation/termination factors, cytosolic aminoacyl-tRNA
785 synthetases, mitochondrial translation factors, and cytosolic and mitochondrial ribosome
786 biogenesis factors. Additionally, six co-translational proteostasis categories were
787 defined: nascent chain chaperones (NAC/RAC), ribosome quality control (RQC),
788 UFMylation, mitochondrial import (TOM/TIM), ER import (SRP/SEC61), and the
789 TRiC/CCT chaperonin. TR breakdown was tested independently of the nine-branch
790 framework. Per-individual signature scores were calculated as the mean z-scored lysate
791 abundance of all detected subcategory members.

792 To assess multicollinearity among proteostasis predictors in joint models, we calculated
793 variance inflation factors (VIF) using the car package in R; all VIF values were below 3,
794 well under the threshold of 5-10 typically considered problematic for coefficient stability.

Acknowledgements

We thank the NIH NeuroBioBank for providing post-mortem brain samples. This research was supported by NIH grants RFAG057358 (G.J.L), and R01AG02963 (G.J.L), the Larry L. Hillblom Foundation LLHF Ctr Supp. and NIA U01AG045844 (G.J.L), the University of Southern California and Buck Institute Nathan Shock Center P30AG068345 (MPI: Verdin, Curran, Cohen, Lithgow) and Cellular Senescence and Beyond Core (Schilling) (E.A), and The Diana Jacob Kalman American Federation for Aging Research (AFAR) Scholarship (E.A).

Ethics Statement

Collection and distribution procedures at each Brain and Tissue Repository are conducted under IRB-approved protocols at their respective institutions. Because this study used de-identified post-mortem tissue, it was determined not to constitute human subjects research and was exempt from additional IRB review.

References

1. López-Otín, C., Blasco, M. A., Partridge, L., Serrano, M. & Kroemer, G. Hallmarks of aging: An expanding universe. *Cell* **186**, 243–278 (2023).

2. Hartl, F. U. Protein Misfolding Diseases. *Annu. Rev. Biochem* **86**, 21–26 (2017).

3. Molzahn, C. *et al.* Shift of the insoluble content of the proteome in the aging mouse brain. *Proceedings of the National Academy of Sciences* **120**, e2310057120 (2023).

4. Reis-Rodrigues, P. *et al.* Proteomic analysis of age-dependent changes in protein solubility identifies genes that modulate lifespan. *Aging Cell* **11**, 120–127 (2012).

5. David, D. C. *et al.* Widespread protein aggregation as an inherent part of aging in C. elegans. *PLoS Biol.* **8**, 47–48 (2010).

6. Kelmer Sacramento, E. *et al.* Reduced proteasome activity in the aging brain results in ribosome stoichiometry loss and aggregation. *Mol. Syst. Biol.* **16**, MSB209596 (2020).

7. Demontis, F. & Perrimon, N. FOXO/4E-BP signaling in Drosophila muscles regulates organism-wide proteostasis during aging. *Cell* **143**, 813–825 (2010).

8. Ross, C. A. & Poirier, M. A. Protein aggregation and neurodegenerative disease. *Nature Medicine 2004 10:7* **10**, S10–S17 (2004).

9. Thibeault, J. *et al.* Sarkosyl: A milder detergent than SDS for identifying proteins with moderately high hyperstability using gel electrophoresis. *Anal. Biochem.* **571**, 21–24 (2019).

10. Mate de Gerando, A. *et al.* Aqueous extractable nonfibrillar and sarkosyl extractable fibrillar Alzheimer's disease tau seeds have distinct properties. *Acta Neuropathol. Commun.* **12**, 145 (2024).

11. Xiong, L.-W., Raymond, L. D., Hayes, S. F., Raymond, G. J. & Caughey, B. Conformational change, aggregation and fibril formation induced by detergent treatments of cellular prion protein. *J. Neurochem.* **79**, 669–678 (2001).

12. Breyer, J. *et al.* Detergents modify proteinase K resistance of PrPSc in different transmissible spongiform encephalopathies (TSEs). *Vet. Microbiol.* **157**, 23–31 (2012).

13. Gozal, Y. M. *et al.* Proteomics Analysis Reveals Novel Components in the Detergent-Insoluble Subproteome in Alzheimer's Disease. *J. Proteome Res.* **8**, 5069–5079 (2009).

838 14. Diner, I., Nguyen, T. & Seyfried, N. T. Enrichment of Detergent-insoluble Protein Aggregates from
839 Human Postmortem Brain. *JoVE* e55835 (2017) doi:doi:10.3791/55835.

840 15. Klucken, J. *et al.* Clinical and biochemical correlates of insoluble α-synuclein in dementia with
841 Lewy bodies. *Acta Neuropathol.* **111**, 101–108 (2006).

842 16. Chang, A. *et al.* Homotypic fibrillization of TMEM106B across diverse neurodegenerative
843 diseases. *Cell* **185**, 1346-1355.e15 (2022).

844 17. Takahashi, M. *et al.* Extracellular association of APP and tau fibrils induces intracellular aggregate
845 formation of tau. *Acta Neuropathol.* **129**, 895–907 (2015).

846 18. Tatzelt, J., Prusiner, S. B. & Welch, W. J. Chemical chaperones interfere with the formation of
847 scrapie prion protein. *EMBO J.* **15**, 6363–6373 (1996).

848 19. Thibeault, J. *et al.* Sarkosyl: A milder detergent than SDS for identifying proteins with moderately
849 high hyperstability using gel electrophoresis. *Anal. Biochem.* **571**, 21–24 (2019).

850 20. Li, L. *et al.* Alzheimer's disease brain contains tau fractions with differential prion-like activities.
851 *Acta Neuropathol. Commun.* **9**, 28 (2021).

852 21. Nizhnikov, A. A. *et al.* Proteomic Screening for Amyloid Proteins. *PLoS One* **9**, e116003- (2015).

853 22. Miyasaka, T. *et al.* Visualization of Newly Deposited tau in Neurofibrillary Tangles and Neuropil
854 Threads. *J. Neuropathol. Exp. Neurol.* **64**, 665–674 (2005).

855 23. Smith, D. P. *et al.* Concentration Dependent Cu2+ Induced Aggregation and Dityrosine Formation
856 of the Alzheimer's Disease Amyloid-β Peptide. *Biochemistry* **46**, 2881–2891 (2007).

857 24. Douglas, P. M. *et al.* Chaperone-dependent amyloid assembly protects cells from prion toxicity.
858 *Proceedings of the National Academy of Sciences* **105**, 7206–7211 (2008).

859 25. Lam, H. T., Graber, M. C., Gentry, K. A. & Bieschke, J. Stabilization of α-Synuclein Fibril Clusters
860 Prevents Fragmentation and Reduces Seeding Activity and Toxicity. *Biochemistry* **55**, 675–685
861 (2016).

862 26. McEwan, W. A. *et al.* Cytosolic Fc receptor TRIM21 inhibits seeded tau aggregation. *Proceedings*
863 *of the National Academy of Sciences* **114**, 574–579 (2017).

864 27. Darricau, M. *et al.* Tau seeds from patients induce progressive supranuclear palsy pathology and
865 symptoms in primates. *Brain* **146**, 2524–2534 (2023).

866 28. Bernis, M. E. *et al.* Prion-like propagation of human brain-derived alpha-synuclein in transgenic
867 mice expressing human wild-type alpha-synuclein. *Acta Neuropathol. Commun.* **3**, 75 (2015).

868 29. Zampar, S., Di Gregorio, S. E., Grimmer, G., Watts, J. C. & Ingelsson, M. “Prion-like” seeding and
869 propagation of oligomeric protein assemblies in neurodegenerative disorders. *Front. Neurosci.*
870 **Volume 18-2024**, (2024).

871 30. Jucker, M. & Walker, L. C. Propagation and spread of pathogenic protein assemblies in
872 neurodegenerative diseases. *Nat. Neurosci.* **21**, 1341–1349 (2018).

873 31. Douglas, P. M. *et al.* Chaperone-dependent amyloid assembly protects cells from prion toxicity.
874 *Proceedings of the National Academy of Sciences* **105**, 7206–7211 (2008).

875 32. Arrasate, M., Mitra, S., Schweitzer, E. S., Segal, M. R. & Finkbeiner, S. Inclusion body formation
876 reduces levels of mutant huntingtin and the risk of neuronal death. *Nature* **431**, 805–810 (2004).

877 33. Tartaglia, G. G. & Vendruscolo, M. The Zyggregator method for predicting protein aggregation
878 propensities. *Chem. Soc. Rev.* **37**, 1395–1401 (2008).

879 34. Sormanni, P. & Vendruscolo, M. Protein solubility predictions using the camsol method in the
880 study of protein homeostasis. *Cold Spring Harb. Perspect. Biol.* **11**, (2019).

881 35. von Bergen, M., Barghorn, S., Biernat, J., Mandelkow, E.-M. & Mandelkow, E. Tau aggregation is
882 driven by a transition from random coil to beta sheet structure. *Biochimica et Biophysica Acta*
883 *(BBA) - Molecular Basis of Disease* **1739**, 158–166 (2005).

884 36. Hardy, J. & Selkoe, D. J. The amyloid hypothesis of Alzheimer’s disease: progress and problems
885 on the road to therapeutics. *Science* **297**, 353–356 (2002).

886 37. Visser, B. S., Lipiński, W. P. & Spruijt, E. The role of biomolecular condensates in protein
887 aggregation. *Nat. Rev. Chem.* **8**, 686–700 (2024).

888 38. Mathieu, C., Pappu, R. V & Taylor, J. P. Beyond aggregation: Pathological phase transitions in
889 neurodegenerative disease. *Science (1979).* **370**, 56–60 (2020).

890 39. Schweighauser, M. *et al.* Age-dependent formation of TMEM106B amyloid filaments in human
891 brains. *Nature 2022 605:7909* **605**, 310–314 (2022).

892 40. Vecchi, G. *et al.* Proteome-wide observation of the phenomenon of life on the edge of solubility.
893 *Proceedings of the National Academy of Sciences* **117**, 1015–1020 (2020).

894 41. Tartaglia, G. G. & Vendruscolo, M. The Zyggregator method for predicting protein aggregation
895 propensities. *Chem. Soc. Rev.* **37**, 1395–401 (2008).

896 42. Fernandez-Escamilla, A.-M., Rousseau, F., Schymkowitz, J. & Serrano, L. Prediction of sequence-
897 dependent and mutational effects on the aggregation of peptides and proteins. *Nat. Biotechnol.*
898 **22**, 1302–1306 (2004).

899 43. Sormanni, P., Aprile, F. A. & Vendruscolo, M. The CamSol Method of Rational Design of Protein
900 Mutants with Enhanced Solubility. *J. Mol. Biol.* **427**, 478–490 (2015).

901 44. Ciryam, P., Kundra, R., Morimoto, R. I., Dobson, C. M. & Vendruscolo, M. Supersaturation is a
902 major driving force for protein aggregation in neurodegenerative diseases. *Trends Pharmacol. Sci.*
903 **36**, 72 (2015).

904 45. Hardenberg, M., Horvath, A., Ambrus, V., Fuxreiter, M. & Vendruscolo, M. Widespread occurrence
905 of the droplet state of proteins in the human proteome. *Proceedings of the National Academy of*
906 *Sciences* **117**, 33254–33262 (2020).

907 46. Monti, M. *et al.* catGRANULE 2.0: accurate predictions of liquid-liquid phase separating proteins at
908 single amino acid resolution. *Genome Biol.* **26**, 33 (2025).

909 47. Consortium, T. U. UniProt: the Universal Protein Knowledgebase in 2025. *Nucleic Acids Res.* **53**,
910 D609–D617 (2025).

911 48. Jumper, J. *et al.* Highly accurate protein structure prediction with AlphaFold. *Nature* **596**, 583–589
912 (2021).

913 49. Kirchner, P. *et al.* Proteome-wide analysis of chaperone-mediated autophagy targeting motifs.
914 *PLoS Biol.* **17**, e3000301- (2019).

915 50. Woltjer, R. L. *et al.* Proteomic determination of widespread detergent insolubility, including Aβ but
916 not tau, early in the pathogenesis of Alzheimer's disease. *The FASEB Journal* **19**, 1923–1925
917 (2005).

918 51. Hales, C. M. *et al.* Changes in the detergent-insoluble brain proteome linked to amyloid and tau in
919 Alzheimer's Disease progression. *Proteomics* **16**, 3042–3053 (2016).

920 52. Kepchia, D. *et al.* Diverse proteins aggregate in mild cognitive impairment and Alzheimer's
921 disease brain. *Alzheimers Res. Ther.* **12**, 75 (2020).

922 53. Guo, Q. *et al.* Targeted Quantification of Detergent-Insoluble RNA-Binding Proteins in Human
923 Brain Reveals Stage and Disease Specific Co-aggregation in Alzheimer's Disease. *Front. Mol.*
924 *Neurosci.* **Volume 14-2021**, (2021).

925 54. Bai, B. *et al.* U1 small nuclear ribonucleoprotein complex and RNA splicing alterations in
926 Alzheimer's disease. *Proceedings of the National Academy of Sciences* **110**, 16562–16567
927 (2013).

928 55. Askenazi, M. *et al.* Compilation of reported protein changes in the brain in Alzheimer's disease.
929 *Nat. Commun.* **14**, 4466 (2023).

930 56. de Geus, M. B., Nairn, A. C., Arnold, S. E. & Carlyle, B. C. A compilation of reported alterations in
931 the cerebrospinal fluid proteome in Alzheimer's disease. *Brain Commun.* **7**, fcaf202 (2025).

932 57. Kim, H. J. *et al.* Mutations in prion-like domains in hnRNPA2B1 and hnRNPA1 cause multisystem
933 proteinopathy and ALS. *Nature* **495**, 467–473 (2013).

934 58. Moujalled, D. *et al.* Phosphorylation of hnRNP K by cyclin-dependent kinase 2 controls cytosolic
935 accumulation of TDP-43. *Hum. Mol. Genet.* **24**, 1655–1669 (2015).

936 59. Vilariño-Güell, C. *et al.* VPS35 Mutations in Parkinson Disease. *The American Journal of Human*
937 *Genetics* **89**, 162–167 (2011).

938 60. Consortium, T. P. *et al.* A Comprehensive Enumeration of the Human Proteostasis Network. 1.
939 Components of Translation, Protein Folding, and Organelle-Specific Systems. *bioRxiv*
940 2022.08.30.505920 (2022) doi:10.1101/2022.08.30.505920.

941 61. Consortium, T. P. *et al.* A Comprehensive Enumeration of the Human Proteostasis Network. 2.
942 Components of the Autophagy-Lysosome Pathway. *bioRxiv* 2023.03.22.533675 (2023)
943 doi:10.1101/2023.03.22.533675.

944 62. McKenzie, A. T. *et al.* Brain Cell Type Specific Gene Expression and Co-expression Network
945 Architectures. *Sci. Rep.* **8**, 8868 (2018).

946 63. Choi, I. *et al.* Microglia clear neuron-released α-synuclein via selective autophagy and prevent
947 neurodegeneration. *Nat. Commun.* **11**, 1386 (2020).

948 64. Sperling, R. A. *et al.* Toward defining the preclinical stages of Alzheimer's disease:
949 Recommendations from the National Institute on Aging-Alzheimer's Association workgroups on
950 diagnostic guidelines for Alzheimer's disease. *Alzheimer's & Dementia* **7**, 280–292 (2011).

951 65. Tanase, M. *et al.* Role of carbonyl modifications on aging-associated protein aggregation. *Sci.*
952 *Rep.* **6**, (2016).

953 66. Xie, X. *et al.* Quantification of insoluble protein aggregation in caenorhabditis elegans during aging
954 with a novel data-independent acquisition workflow. *Journal of Visualized Experiments* **2020**, 1–17
955 (2020).

956 67. Hong, S. *et al.* Dynamic Analysis of Amyloid β-Protein in Behaving Mice Reveals Opposing
957 Changes in ISF versus Parenchymal Aβ during Age-Related Plaque Formation. *The Journal of*
958 *Neuroscience* **31**, 15861 (2011).

959 68. Kawaguchi, Y. *et al.* The Deacetylase HDAC6 Regulates Aggresome Formation and Cell Viability
960 in Response to Misfolded Protein Stress. *Cell* **115**, 727–738 (2003).

961 69. Zatloukal, K. *et al.* p62 Is a Common Component of Cytoplasmic Inclusions in Protein Aggregation
962 Diseases. *Am. J. Pathol.* **160**, 255–263 (2002).

963 70. Gamerdinger, M., Kaya, A. M., Wolfrum, U., Clement, A. M. & Behl, C. BAG3 mediates
964 chaperone-based aggresome-targeting and selective autophagy of misfolded proteins. *The EMBO*
965 *Reports* **12**, 149–156 (2011).

966 71. Banani, S. F., Lee, H. O., Hyman, A. A. & Rosen, M. K. Biomolecular condensates: organizers of
967 cellular biochemistry. *Nat. Rev. Mol. Cell Biol.* **18**, 285–298 (2017).

968 72. Sacramento, E. K. *et al.* Reduced proteasome activity in the aging brain results in ribosome
969 stoichiometry loss and aggregation. *Mol. Syst. Biol.* **16**, 9596 (2020).

970 73. Walther, D. M. *et al.* Widespread proteome remodeling and aggregation in aging C. elegans. *Cell*
971 **161**, 919–932 (2015).

972 74. Wang, X. & Chen, X. J. A cytosolic network suppressing mitochondria-mediated proteostatic
973 stress and cell death. *Nature* **524**, 481–484 (2015).

974 75. Mielke, M. M., Vemuri, P. & Rocca, W. A. Clinical epidemiology of Alzheimer's disease: Assessing
975 sex and gender differences. *Clinical Epidemiology* vol. 6 37–48 Preprint at
976 https://doi.org/10.2147/CLEP.S37929 (2014).

977 76. Mielke, M. M., Ferretti, M. T., Iulita, M. F., Hayden, K. & Khachaturian, A. S. Sex and gender in
978 Alzheimer's disease – Does it matter? *Alzheimer's & Dementia* **14**, 1101–1103 (2018).

979 77. Félix-Redondo, F. J., Grau, M. & Fernández-Bergés, D. Cholesterol and cardiovascular disease in
980 the elderly. Facts and gaps. *Aging Dis.* 154–169. (2013).

981 78. Collins, B. C. *et al.* Multi-laboratory assessment of reproducibility, qualitative and quantitative
982 performance of SWATH-mass spectrometry. *Nat. Commun.* **8**, 291 (2017).

983 79. Bruderer, R. *et al.* Optimization of Experimental Parameters in Data-Independent Mass
984 Spectrometry Significantly Increases Depth and Reproducibility of Results *. *Molecular & Cellular*
985 *Proteomics* **16**, 2296–2309 (2017).

986 80. Gillet, L. C. *et al.* Targeted Data Extraction of the MS/MS Spectra Generated by Data-independent
987 Acquisition: A New Concept for Consistent and Accurate Proteome Analysis * . *Molecular &*
988 *Cellular Proteomics* **11**, (2012).

989 81. Burger, T. Gentle Introduction to the Statistical Foundations of False Discovery Rate in
990 Quantitative Proteomics. *J. Proteome Res.* **17**, 12–22 (2018).

991 82. Kolberg, L. *et al.* g:Profiler—interoperable web service for functional enrichment analysis and gene
992 identifier mapping (2023 update). *Nucleic Acids Res.* **51**, W207–W212 (2023).

993 83. Sutton, G. J. *et al.* Comprehensive evaluation of deconvolution methods for human brain gene
994 expression. *Nat. Commun.* **13**, 1358 (2022).

995 84. Rath, S. *et al.* MitoCarta3.0: an updated mitochondrial proteome now with sub-organelle
996 localization and pathway annotations. *Nucleic Acids Res.* **49**, D1541–D1547 (2021).

997

998

Table 1. Functional classification of sarkosyl-insoluble accumulators (n = 303)

Functional category	n	Proteins
Cytoskeletal		
Actin cytoskeleton & cell adhesion	41	*ABLIM2, ACTN1, ACTN2, ADD1, AFDN, AHNAK, AHNAK2, ANK2, CORO1A, CORO1C, CRACDL, CRKL, CTNNA2, CTTN, DBNL, DIAPH1, DMTN, DST, FMN2, FSCN1, GSN, ITGB4, LASP1, LIMCH1, LPP, MICA PALM, PLEC, PLEKHA6, PPP1R12A, SORBS1, SORBS2, TAGLN3, TJP1, TJP2, TLN2, TNS3, TPPP, TW VIM, WDR1*
Microtubule & motor proteins	15	*ATCAY, C1orf198, CCDC6, CEP170, DCTN2, DCTN4, DYNC1I1, KLC4, KRT86, LZTFL1, MAPRE3, PAFA TACC1, TBCB, TBCC*
Synaptic		
Postsynaptic scaffolding & signaling	23	*AKAP12, BAIAP2, BAIAP3, CTNND2, DBN1, DLG4, GUCY1A1, HOMER1, ITPR1, ITPR2, MAGI2, MAP2, PDE2A, PLCD1, PLXNA1, PRKAR2B, PTK2B, RTN1, RTN3, RTN4, SIPA1L1, SYNPO, TNIK*
Presynaptic machinery	13	*CADPS2, DNM1, DNM3, GAD2, NECAB1, PTPRN, SCRN1, SH3GL3, STXBP1, SYN1, SYN2, SYN3, SYN*
14-3-3 proteins	6	*YWHAB, YWHAE, YWHAG, YWHAH, YWHAQ, YWHAZ*
Dystrophin-associated complex	5	*DTNA, DTNB, SNTA1, SNTB1, SNTB2*
Mitochondrial		
Energy metabolism	28	*ACAD9, ACO2, ALDH18A1, ALDH6A1, BCKDHA, CHDH, CPT2, CRAT, CYP27A1, DDAH2, DECR2, DGL DLAT, GLS, HSD17B10, IDH2, LDHD, MCCC1, MMUT, NDUFS1, NFS1, NIT1, OGDH, OGDHL, OXCT1, P PDPR, SUCLA2*
Proteostasis & import	8	*AFG3L2, GRPEL1, HSPA9, PPIF, SPRYD4, TOMM34, TOMM70, TRAP1*
RNA & translation	7	*DARS2, HARS2, MRPS27, PUS1, SARS2, SLIRP, SUPV3L1*
Membrane trafficking		
Endosomal trafficking	26	*AAK1, AP1G1, AP1M1, APPL1, APPL2, AVL9, EHD3, EPN1, EPS15, EPS15L1, GGA3, HGS, ITSN1, NEC PDCD6IP, PTPN23, RBSN, RELCH, SGIP1, SGSM1, SPART, STAM2, TOM1, VPS26B, VPS29, VPS35*
ER & secretory pathway	10	*ARHGAP5, FAM126B, NRBP1, PCYT2, PREPL, SACM1L, SEC16A, SEC31A, TMED8, USO1*
Proteostasis		
Ubiquitin-proteasome system	13	*F8A1, NSFL1C, OTUB1, PLAA, PSMF1, RAD23A, UBA1, UBE4A, UBLCP1, UCHL1, USP14, USP25, USP*
Cytosolic chaperones	12	*BAG3, DNAJB1, FKBP1A, FKBP4, HSP90AA1, HSP90AB1, HSPA4L, HSPB1, HSPB8, PPIA, SGTB, SUG*
Autophagy & selective clearance	7	*CTSD, MAP1S, PIP4K2B, PPT1, SMCR8, SQSTM1, WDR81*
Metabolism & redox		
Lipid & small molecule metabolism	17	*ATIC, CKB, CMBL, CNDP2, FASN, GPI, NAGK, OLA1, PAFAH1B3, PDXK, PEX19, PGAM1, PITPNM3, PP PREP, RAP1GDS1, TKT*
Redox & detoxification	10	*AKR1A1, CBR1, CCS, GATD3B, GCLC, GSTM3, GSTM5, NCOA7, OXR1, TXNRD1*
RNA & translation		
RNA-binding & mRNA processing	13	*ADAR, ELOB, HNRNPA2B1, HNRNPK, HNRNPL, LARP1, RBM14, SND1, TNPO1, UPF2, XPO7, XPOT, ZC3HAV1*
Translation machinery	9	*AARS1, EIF3CL, EIF4A2, EIF4H, EIF5, FARSA, HARS1, LRRC47, YARS1*
Signaling & regulation		
Kinase/phosphatase & signaling	11	*CARM1, GNB2, ITPKB, MAPK3, OGA, PPM1F, PRMT1, PTPA, REPS2, RPS6KA2, STRN3*
Small GTPase regulation	11	*ARHGAP26, ARHGDIA, C2CD5, CDC42EP4, PSD2, PSD3, RABGGTA, RALGAPA1, RAP1GAP2, RASA1 TIAM2*
Other		
Collagen & extracellular matrix	5	*COL18A1, COL1A1, COL6A2, COL6A3, HSPG2*
Glial-associated	4	*ALDH1L1, AQP4, MLC1, RLBP1*
Immune response	4	*BTN3A3, IFIT1, IFIT3, LYSMD2*
Unknown	3	*PHYHD1, PHYHIPL, WDR17*
Disease-associated aggregation	2	*HTT, TMEM106B*

Proteins reaching significance ($q < 0.05$, Geriatric vs Young) in the sarkosyl-insoluble fraction were assigned to non-overlapping functional categories based on GO annotations and manual curation.

Figure 1: Brain aging causes proteome-wide, asymmetric remodeling of the insoluble aggregate proteome

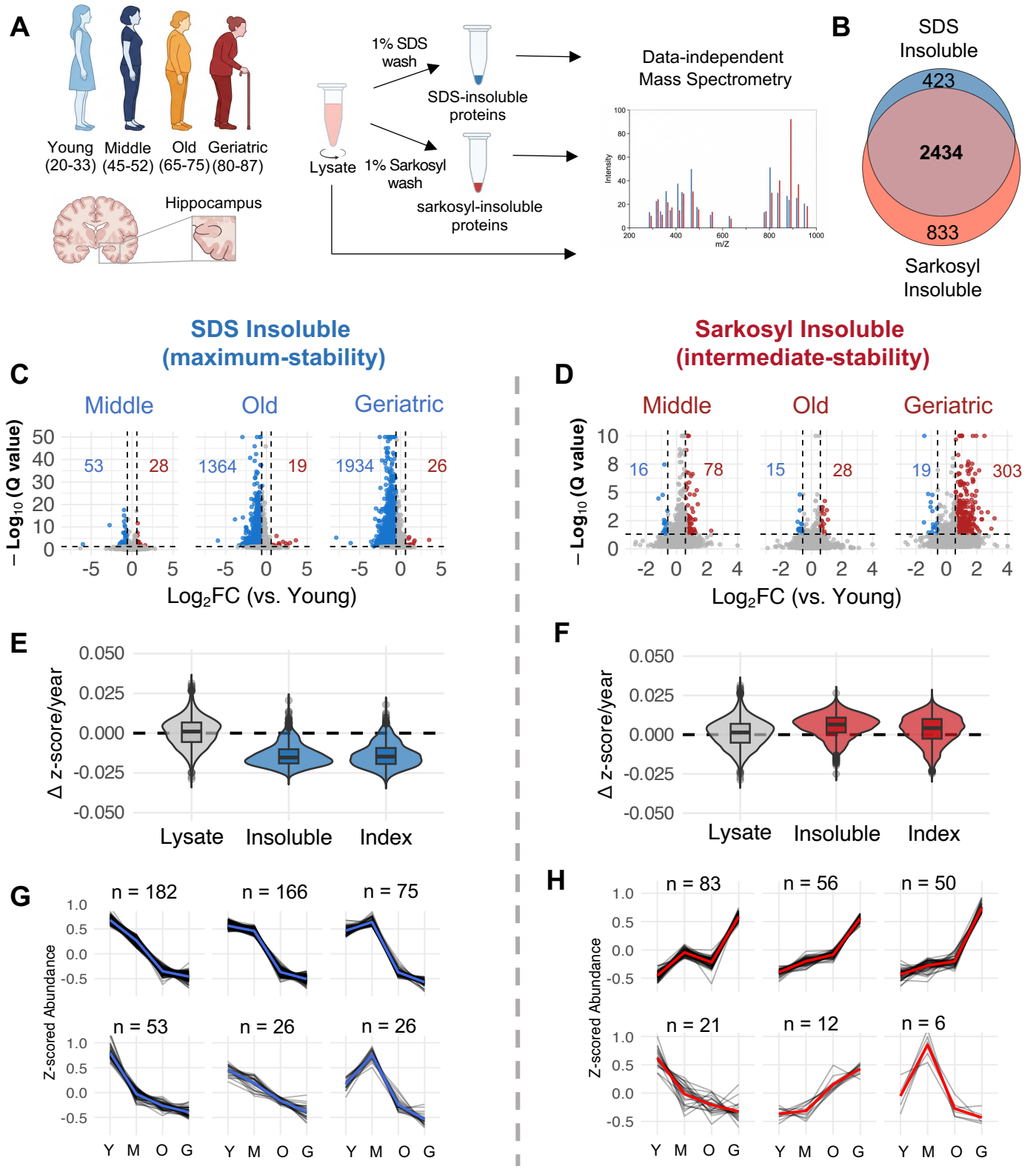

Figure 1: Brain aging causes proteome-wide, asymmetric remodeling of the insoluble aggregate proteome. A. Schematic representation of subject ages, insoluble protein fractionation with mass spec. workflow. **B.** Overlap of detected insoluble proteins in each fraction. **C.** Volcano plots of SDS insoluble protein abundance Log_2(Fold Change) for young (n=12) vs. middle (n=12), vs. old (n=14), and vs. geriatric (n=14), Storey method with paired t-tests and p-values corrected for multiple testing using group-wise testing corrections, significance = $|Log_2(FC)| > 0.58$, $Q < 0.05$). **D.** As in (C) with Sarkosyl insoluble protein abundance, n: young=9, middle=9, old=9, geriatric =11. **E.** Δ z score average change in abundance per year for every protein in lysate, SDS insoluble pellet and SDS insoluble index (insoluble / lysate). **F.** As in (E) with Sarkosyl insoluble proteome. **G.** Clustered trajectories of age-changing SDS insoluble proteins (k = 6). H. As in (G) with Sarkosyl insoluble proteome.

Figure 2: Liquid-liquid phase separation and intrinsic aggregation properties define aggregation state changes during brain aging

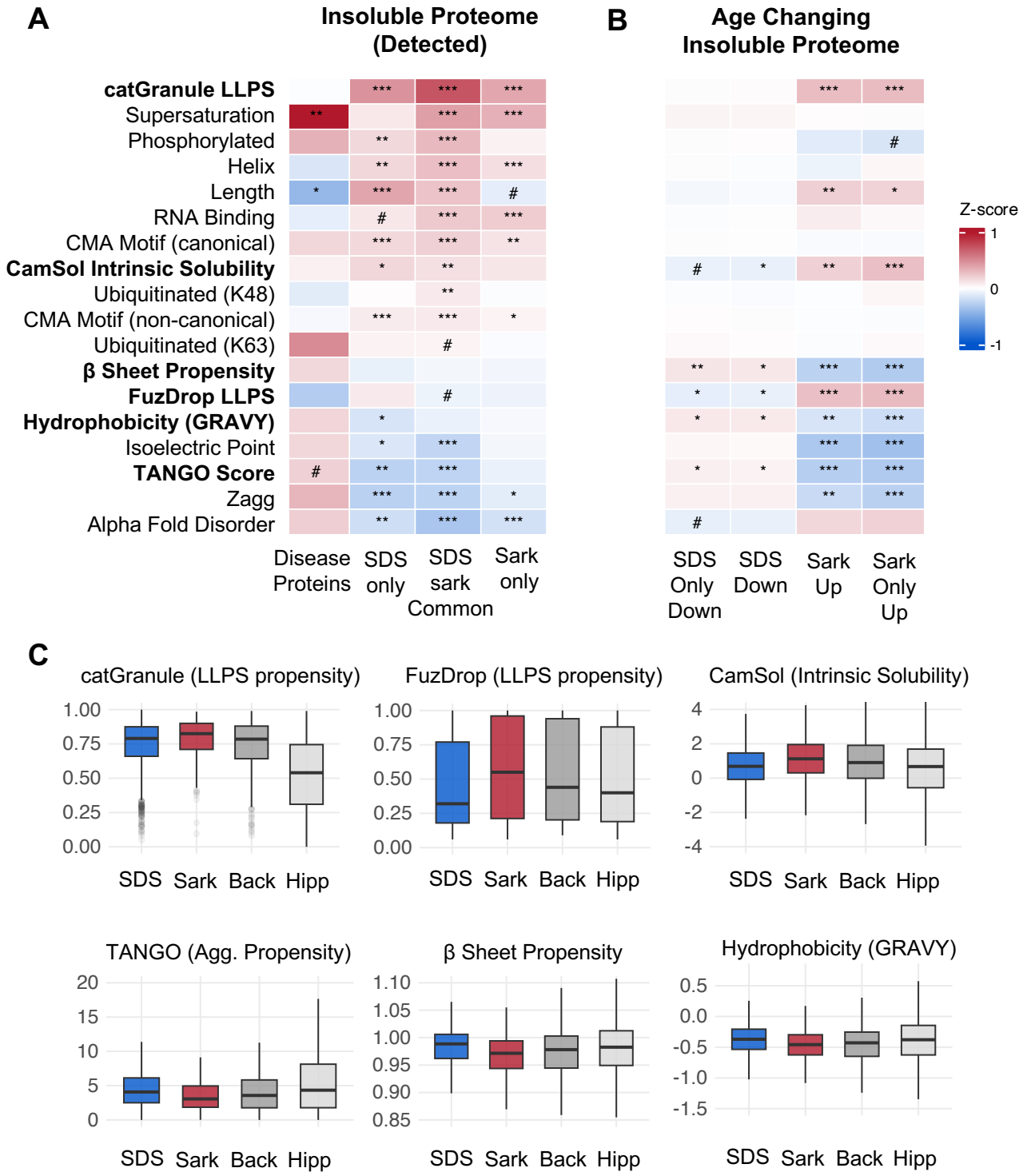

Figure 2: Liquid-liquid phase separation and intrinsic aggregation properties define aggregation state changes during brain aging. A. Heatmap showing enrichment of biophysical and functional features amongst insoluble proteins compared to the hippocampal proteome. Z-scores calculated as the difference between group and background central tendency (mean or median), normalized by background dispersion. Continuous variables: Welch's t-test with Hedges' g effect size (normal distribution) or Wilcoxon rank-sum test with Cliff's delta (non-normal dist.), all use Benjamini-Hochberg FDR correction **B.** As in (A) with enrichment of age-changing proteins compared to insoluble detected proteins (non-changing). **C.** Boxplots for select features that show significant effects in the sarkosyl age-changing group. Extreme outlier proteins represented by grey points. Back = Insoluble detected proteins in SDS and Sarkosyl. Hipp – Hippocampal proteome. ***q < 0.001, **q < 0.01, *q < 0.05, #q <0.1.

Figure 3: Proteins that accumulate in sarkosyl-insoluble aggregates are enriched with AD plaque, tangle and CSF proteins

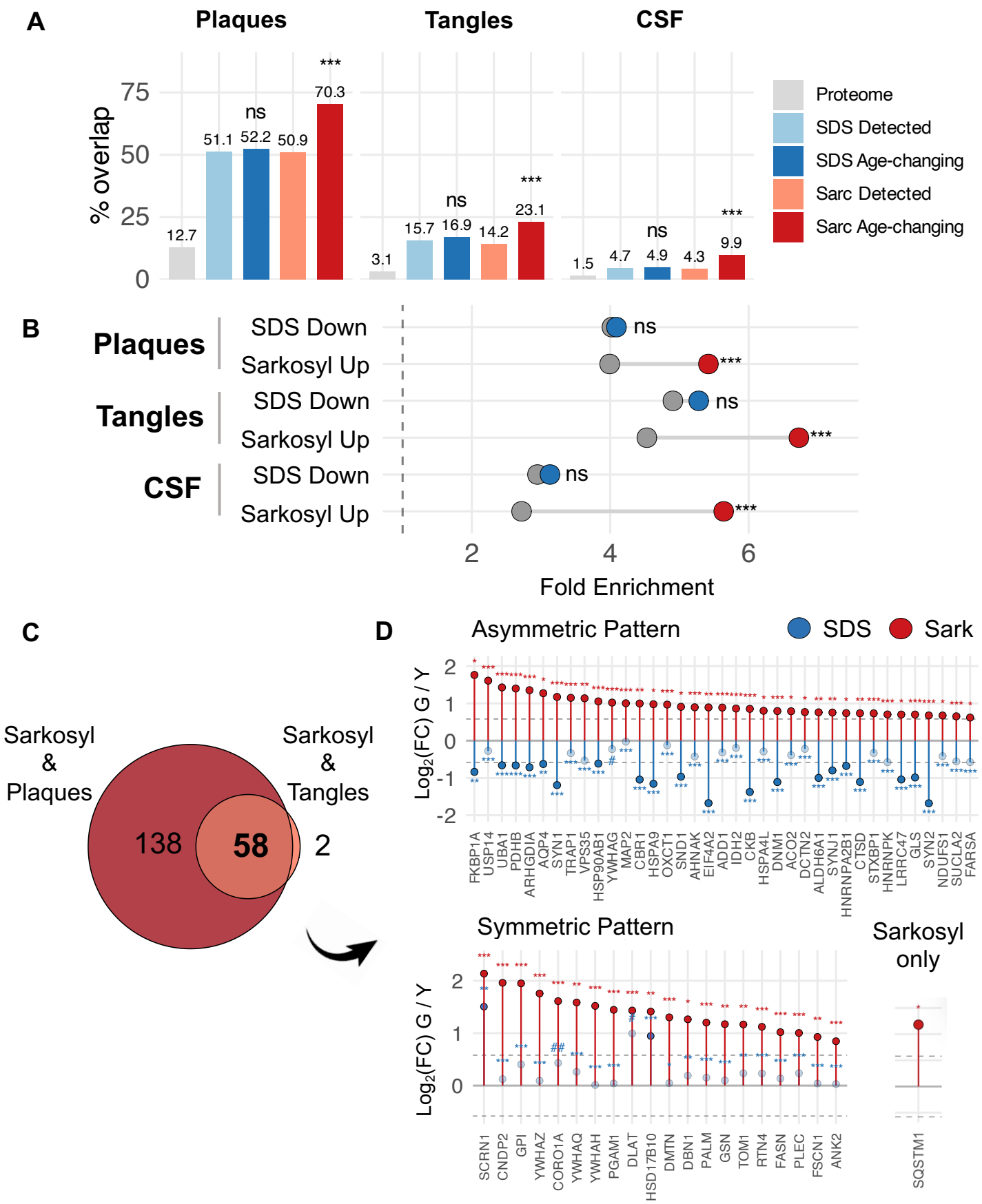

Figure 3: Proteins that accumulate in sarkosyl-insoluble aggregates are enriched with AD plaque, tangle and CSF proteins A. Barplots showing percentage of insoluble proteome common with AD plaques, tangles, and CSF biomarkers. Proteome = Hippocampal proteome, Fischer's exact test. **B.** Forest plot showing fold enrichment of insoluble proteome in AD plaques, tangles, and CSF biomarkers. Grey = insoluble detected, Blue = SDS age-changing proteins, Red = Sarkosyl age-changing proteins, Fisher's exact test. **C**. Overlap of sarkosyl accumulators with plaques and tangles. **D** lolipop plots showing Log_2(Fold Change) using geriatric vs young comparison for the 58 insoluble proteins common to sarkosyl accumulation, plaques and tangles. Blue = SDS, Red = Sarkosyl. Solid circle = significant, open circle = not significant. ***q < 0.001, **q < 0.01, *q < 0.05, #q <0.1, ##q <0.2,

Figure 4: Mitochondrial and synaptic proteins accumulate in sarkosyl insoluble aggregates during brain aging

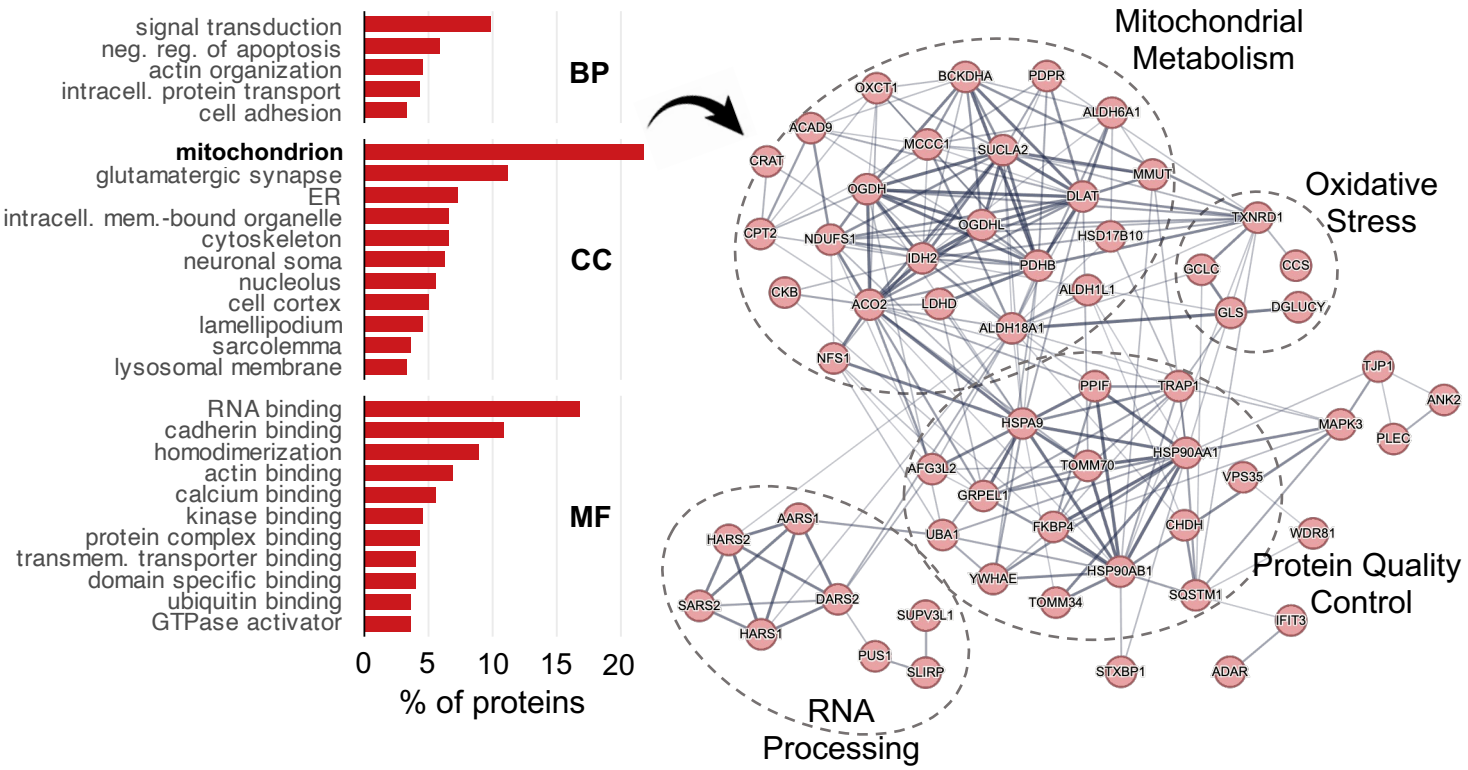

Figure 4: Mitochondrial and synaptic proteins accumulate in sarkosyl insoluble aggregates during brain aging. **A**. Barplots showing proportion of sarkosyl accumulating proteins across functional GO categories. **B**. STRING protein-protein interaction network diagram showing sarkosyl accumulating mitochondrial proteins.

Figure 5: Proteostasis network capacity and cell type composition predict individual insoluble protein burden

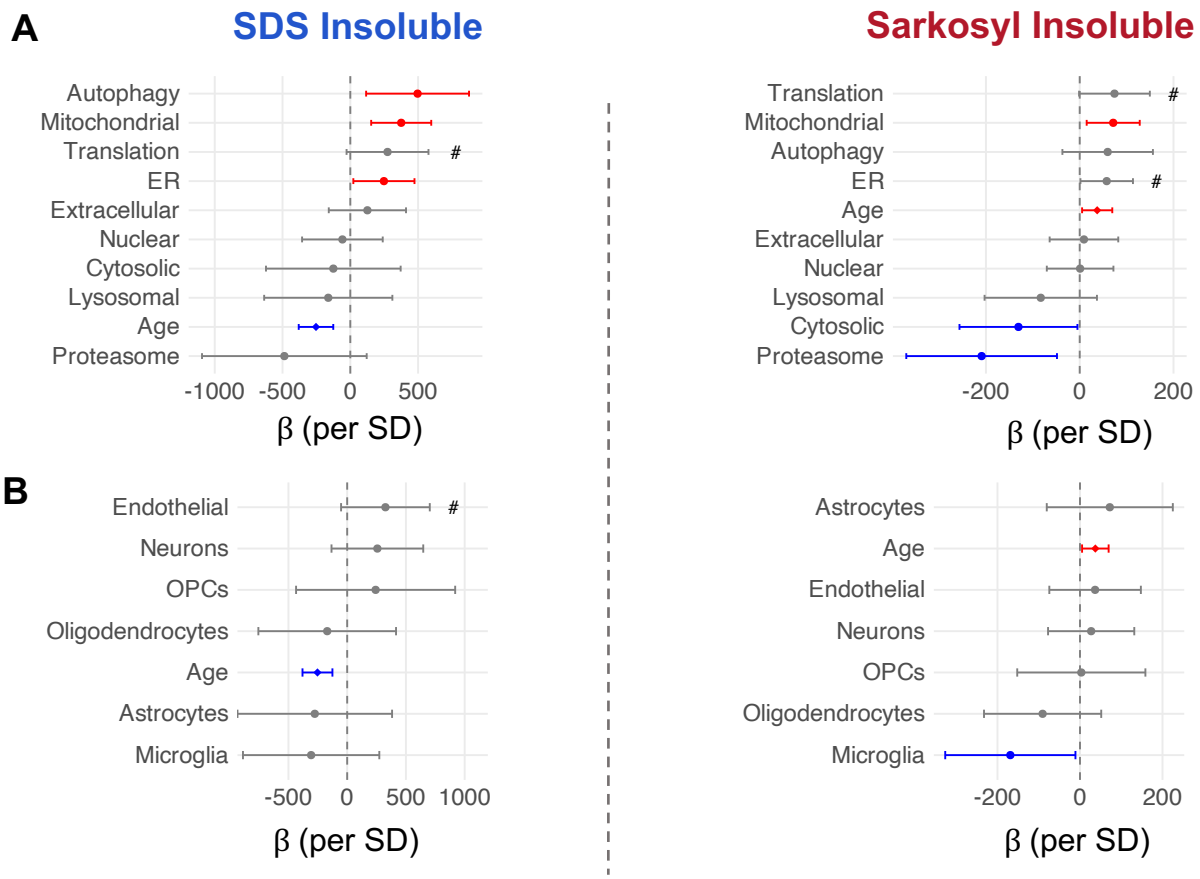

Figure 5. Proteostasis network capacity and cell type composition predict individual insoluble protein burden. **A** Forest plots showing the association between lysate-level proteostasis branch signature scores and the burden of age-changing insoluble proteins Left = SDS, Right = Sarkosyl. Points show the beta coefficient +/- 95% confidence interval from a linear model adjusting for age (insol. burden ~ age + predictor), Red = significant positive predictor, Blue = significant negative predictor. **B.** As in (A), age-adjusted linear model but using cell type signature scores and insoluble burden. OPC = Oligodendrocyte Precursor Cells, #p <0.1.

Supplementary Figure 1

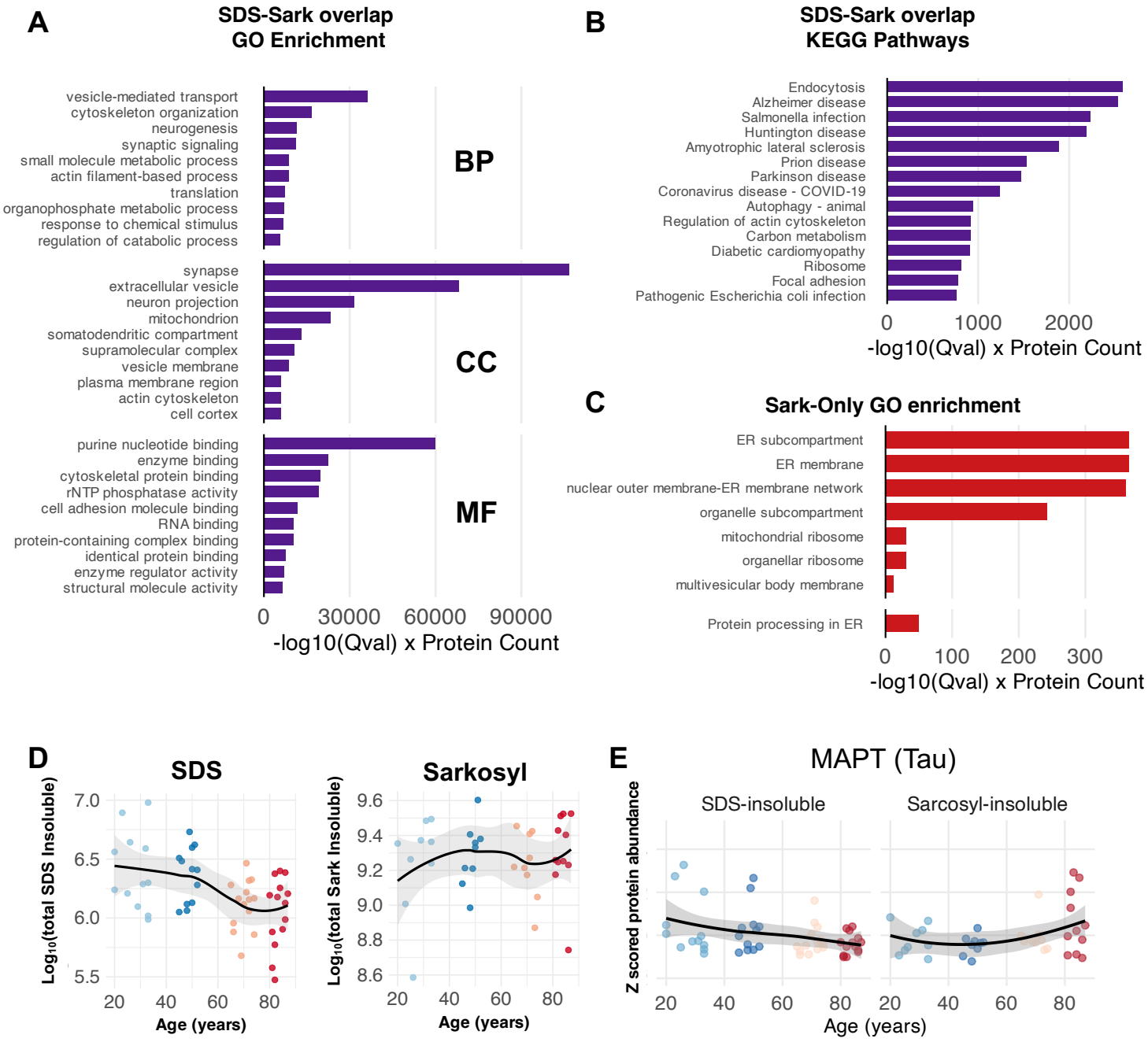

A. Barplot of top enriched GO terms for insoluble proteins common to both SDS and Sarkosyl fractions compared against the hippocampal proteome background, all q<0.05, Fisher's one-tailed test with Benjamini-Hochberg FDR correction. **B** As in (A) with top enriched KEGG pathway terms. **C.** Barplot of top enriched GO terms for insoluble proteins measured exclusively in the Sarkosyl fraction compared against the Sarkosyl insoluble detected as background, all q<0.05, Fisher's one-tailed test with Benjamini-Hochberg FDR correction. **D.** Loess plots of Log_{10}(Total Insoluble Signal) against subject age for SDS insoluble proteome (left) and Sarkosyl insoluble proteome (right), each data point represents an independent biological sample (individual donor). **E.** Loess plots of z-scored insoluble Tau protein abundance against subject age for SDS (left) and Sarkosyl (right), each data point represents an independent biological sample (individual donor).

Supplementary Figure 2

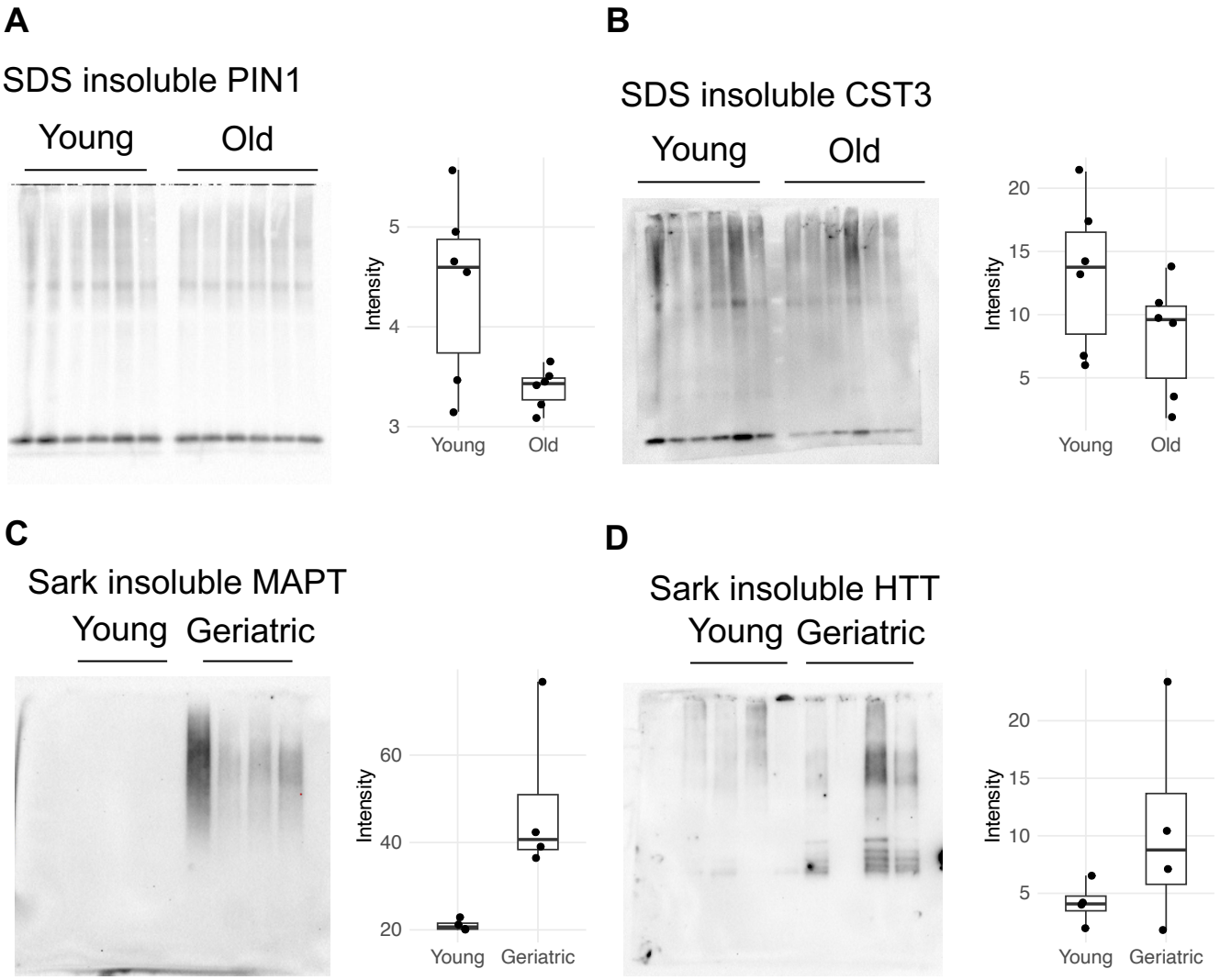

A. Western blot of SDS insoluble PIN1, 6 young and 6 old. **B**. Western blot of SDS insoluble CST3, 6 young and 6 old. **C**. Western blot of Sarkosyl insoluble MAPT (Tau), 4 young and 4 geriatric. **D**. Western blot of sarkosyl insoluble HTT, 4 young and 4 geriatric. For all blots each lane represents an independent biological sample (individual donor).

Supplementary Figure 3

A

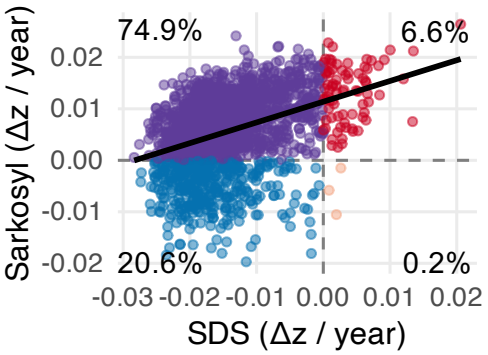

A Scatter plot for all proteins detected in both fractions showing Δz-score mean change over aging in the Sarkosyl fraction and SDS fraction. Spearman correlation line shows positive correlation.

Supplementary Figure 4

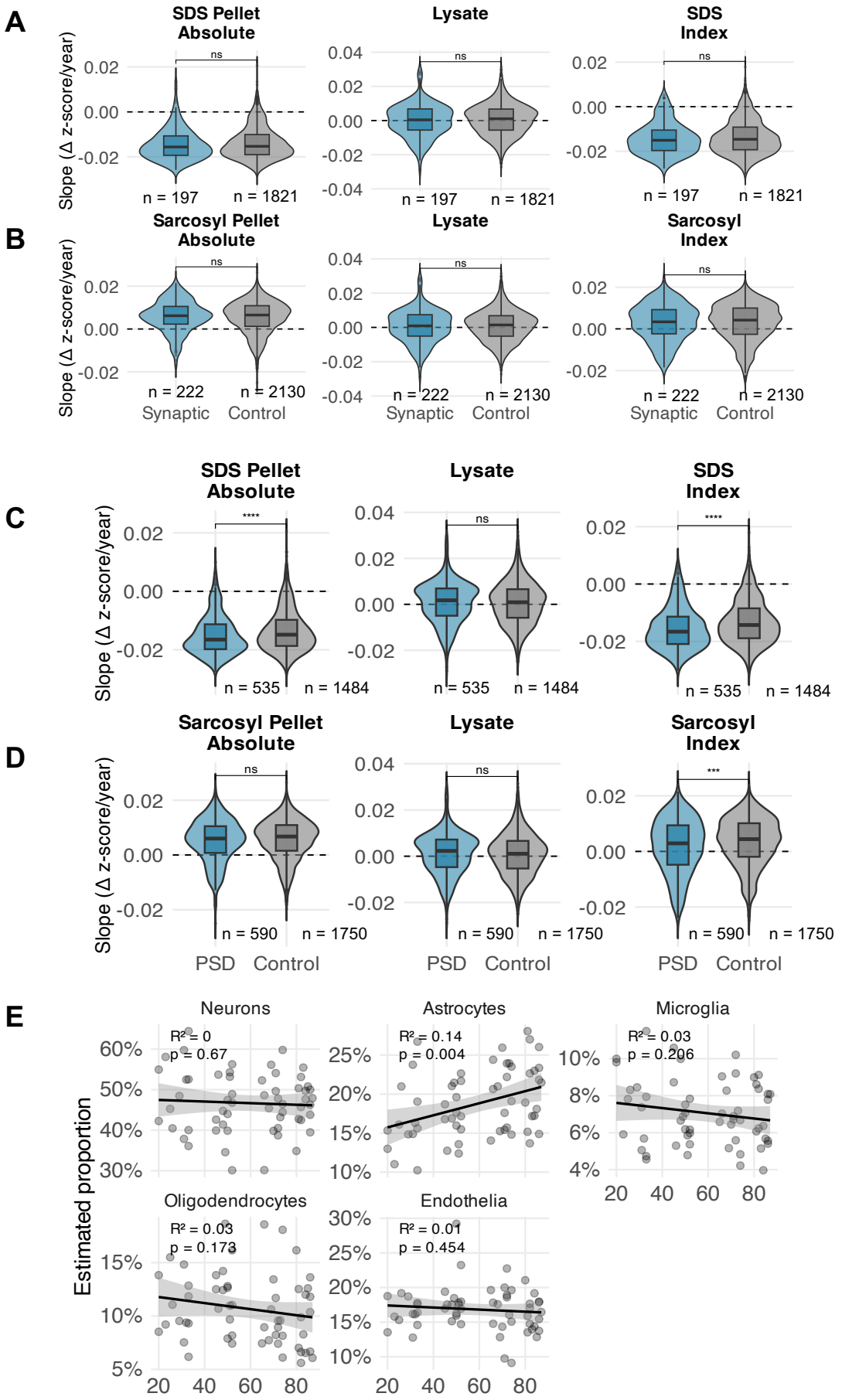

A Violin plot showing Δz-score mean change over aging for synaptic SDS insoluble proteins vs SDS insoluble detected proteins in terms of abundance in the pellet, abundance in the lysate, and the insolubility index (pellet / lysate), Mann Whitney U test. **B**. As in (A) with synaptic Sarkosyl insoluble proteins. **C-D**. As in (A-B) with post-synaptic density (PSD) insoluble proteins, Mann Whitney U test. **E.** Cell type proportion estimates for major central nervous system cell types. Pearson correlation analysis, estimated using dTangle and multibrain human reference signature, each data point represents an independent biological sample (individual donor).

Supplementary Figure 5

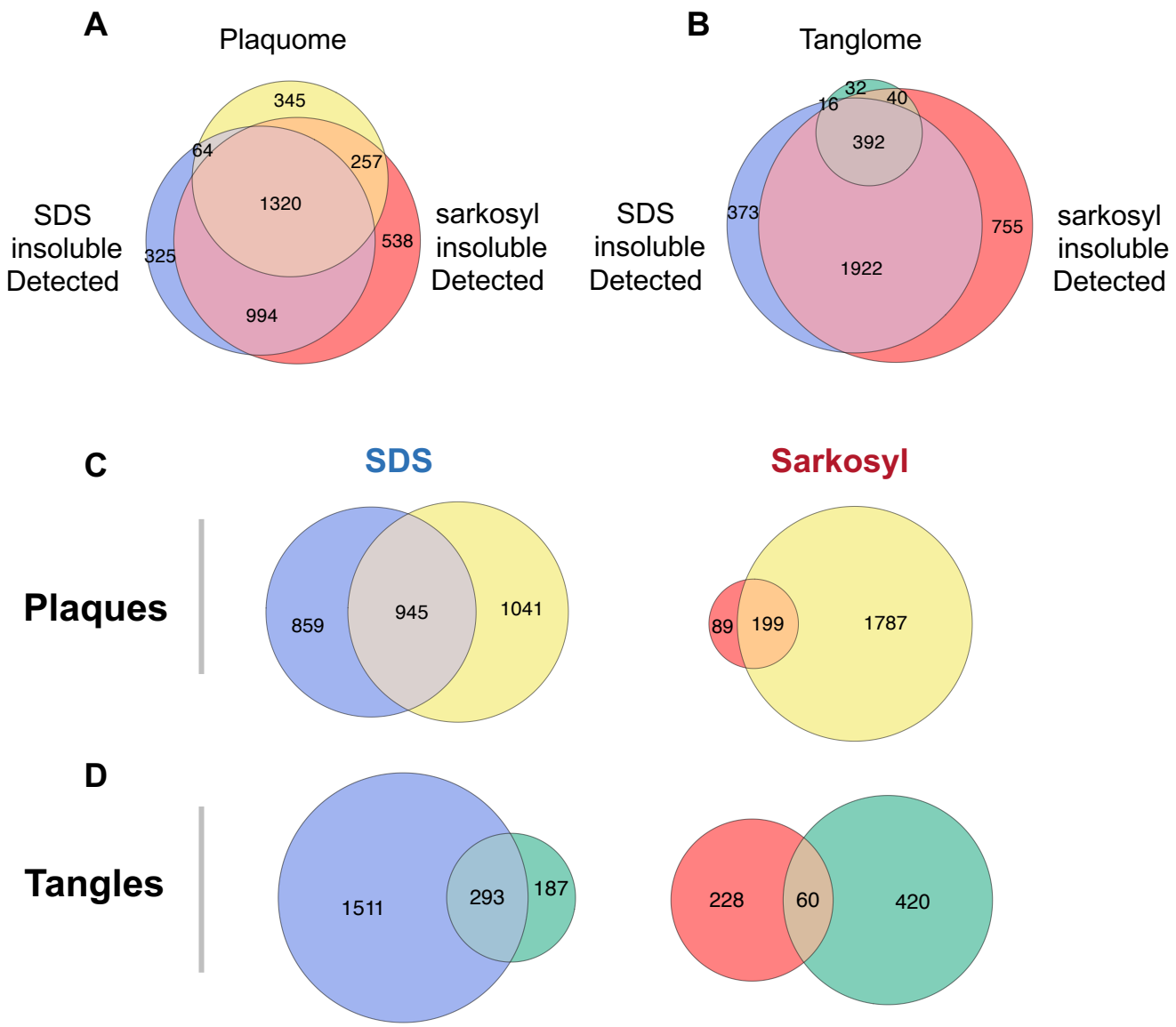

A Overlap between detected insoluble proteomes and plaquome. **B** Overlap between detected insoluble proteomes and tangleome. **C**. Overlap between age-changing proteins and plaqueome for SDS insoluble proteins (left) and Sarkosyl insoluble proteins (right). **D** As in © with tangleome for both fractions. Yellow = plaques, Green = Tangles, Blue = SDS, Red = Sarkosyl.

Supplementary Figure 6

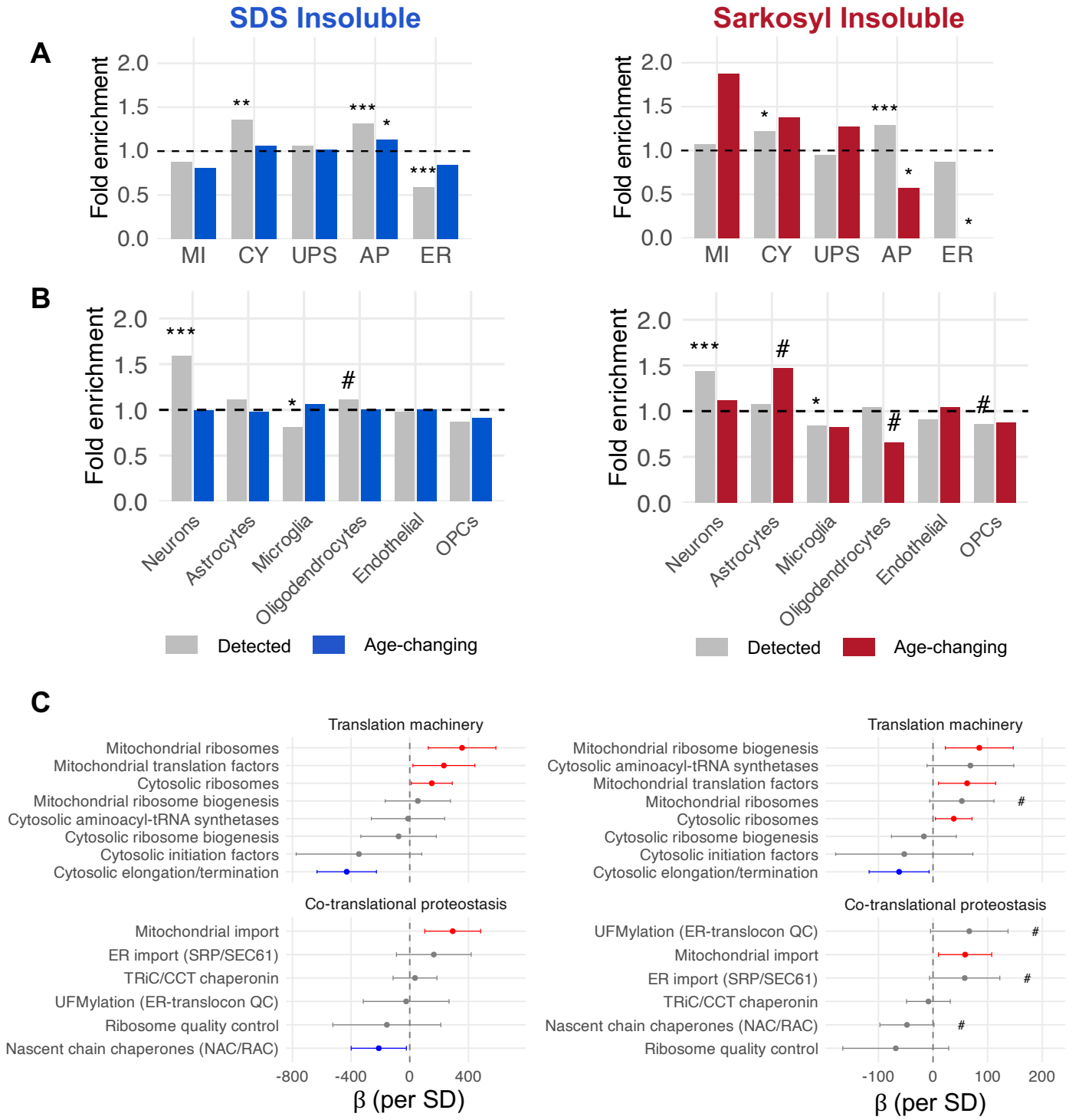

A Fold enrichment of proteostasis branch proteins in the insoluble proteome, Left = SDS, Right = Sarkosyl (Grey bars: insoluble detected, Blue: SDS age-changing, Red: Sarkosyl age-changing. **B** As in A, fold enrichment but using cell type signature scores and insoluble burden. Fisher's exact test with Benjamini-Hochberg correction. **C.** Forest plots showing β coefficient of age-adjusted linear models for translation-associated proteostasis network branch broken down into sub-branches left = SDS, right = Sarkosyl. Points show the beta coefficient +/- 95% confidence interval from a linear model adjusting for age (insol. burden ~ age + predictor). Red: significant positive ($p < 0.05$); Blue: significant negative ($p < 0.05$); grey, non-significant. # = $p<0.1$. MI = mitochondrial, CY = cytoplasmic, UPS = proteasomal, AP = autophagy. ***$q < 0.001$, **$q < 0.01$, *$q < 0.05$, #$q <0.1$. QC = Quality Control.